

## Ultra-Low Voltage Bipolar Hydrogen Production from Biomass-Derived Aldehydes and Water in Membrane-Less Electrolyzers

Hengzhou Liu,<sup>‡a</sup> Naveen Agrawal,<sup>‡b</sup> Arna Ganguly,<sup>‡c</sup> Yifu Chen,<sup>a</sup> Jungkuk Lee,<sup>a</sup> Jiaqi Yu,<sup>d</sup> Wenyu Huang,<sup>d</sup> Mark Mba Wright,<sup>\*c</sup> Michael J. Janik,<sup>\*b</sup> Wenzhen Li<sup>\*a</sup>

<sup>a</sup> *Department of Chemical & Biological Engineering, Iowa State University, Ames, IA 50011, USA.*

<sup>b</sup> *Department of Chemical Engineering, Pennsylvania State University, State College, PA 16801, USA.*

<sup>c</sup> *Department of Mechanical Engineering, Iowa State University, Ames, IA 50011, USA.*

<sup>d</sup> *Department of Chemistry, Iowa State University, Ames, IA 50011, USA.*

‡ These authors contributed equally to this work.

Corresponding authors. [wzli@iastate.edu](mailto:wzli@iastate.edu), [mjj13@psu.edu](mailto:mjj13@psu.edu), [markmw@iastate.edu](mailto:markmw@iastate.edu)

# Table of Contents

Table of Contents .....	2
Experimental Section .....	3
1. Chemicals and materials .....	3
2. Electrode preparation .....	3
3. CuOx reduction by aldehydes in the batch reactor .....	4
4. Electrochemical measurements in the H-type cell .....	4
5. Electrochemical measurements in the MEA-based flow electrolyzer .....	4
6. Membrane characterization .....	5
7. Product analysis .....	6
8. Materials characterization .....	7
9. Calculation of Nernstian equilibrium shift .....	7
10. DFT calculations .....	8
Supplementary Figures (S1–S51) and Tables (S1-S19) .....	10
Supplementary note 1 .....	21
Supplementary note 2 .....	31
Supplementary note 3 .....	35
Techno-economic analysis (TEA) .....	47
References .....	54

## Experimental Section

### 1. Chemicals and materials

Potassium hydroxide (85%), 5-(hydroxymethyl)furfural (HMF, 99%), furfural (99%), furfural alcohol (FA, 98%), 2-furoic acid (98%), acetaldehyde ( $\geq 99.5\%$ ), formaldehyde solution (ACS reagent, 37 wt.% in H<sub>2</sub>O), urea ( $\geq 98\%$ ), NaH<sub>2</sub>PO<sub>4</sub>·H<sub>2</sub>O ( $\geq 99\%$ ), ammonium fluoride ( $\geq 99.99\%$ ), nickel nitrate hexahydrate ( $\geq 97\%$ ), and copper nanoparticles (25 nm) were purchased from Sigma-Aldrich. Acetonitrile (CH<sub>3</sub>CN, HPLC grade), platinum foil (0.025 mm thick, 99.9%), nickel foil (0.1 mm thick, 99.5%), palladium foil (0.025 mm thick, 99.9%), gold foil (0.05 mm thick, 99.95%) were purchased from Fisher Scientific. Silver foil (0.5 mm thick, 99.9985%) was purchased from Alfa Aesar. Nickel foam (1.6 mm thick, purity >99.99%, porosity  $\geq 95\%$ ) was purchased from MTI corporation. Copper foam (130 ppi, 1 mm thick) was purchased from Taobao. Cu<sub>2</sub>O nanoparticles (18 nm, 99.86%) was purchased from US-Nano. Ag<sub>2</sub>O nanoparticles (99+%) CuO nanoparticles (97%) were purchased from Acros Organics. Plain carbon cloth was purchased from the Fuel Cell Store. 40 wt.% Pt on Vulcan XC-72 (Pt/C), IrO<sub>2</sub> powder, and RuO<sub>2</sub> powder were purchased from Premetek. A201 anion exchange membrane was purchased from Tokuyama Corp. 1 cm<sup>2</sup> and 25 cm<sup>2</sup> water electrolyzer hardware were purchased from Shanghai Keqi Tech. and Dioxide Materials, respectively. Silicon gasket (1/16 inch thick) was purchased from McMaster-Carr. H<sub>2</sub> calibration gases (10 ppm, 100 ppm, 1,000 ppm, 5,000 ppm, 10,000 ppm, balance helium) were purchased from Cal Gas Direct. Deionized (DI) water (18.2 M $\Omega$  cm, Barnstead™ E-Pure™) was used for all experiments in this work. All electrochemical tests were performed by a Biologic SP-300 potentiostat with a  $\pm 2$  A/ $\pm 30$  V booster.

### 2. Electrode preparation

The copper foam was first sonicated in 2 M HCl solution for 5 min to remove the surface oxide, followed by rinsing and sonicating in DI-water. The cleaned Cu foam was then sonicated (operating frequency 35 kHz, RF-power 90 W) in the solution of AgNO<sub>3</sub> (50 mM) at room temperature for 30 s to etch and oxidize the Cu surface, and to galvanically exchange Ag with Cu in order to form the as-synthesized CuAg<sub>glv</sub>/Cu electrode. Finally, an oxide-derived CuAg<sub>glv</sub>/Cu was obtained from *in-situ* electroreduction at the potential of  $-0.1$  V<sub>RHE</sub> for 3 min.

CuAg electrodes from electrodeposition (CuAg<sub>dep</sub>/Cu) were prepared based on a previous work.<sup>1</sup> The pre-cleaned Cu foam with 1 cm<sup>2</sup> geometric area was immersed in a 1.5 M H<sub>2</sub>SO<sub>4</sub> aqueous solution containing metal-salt precursors (CuSO<sub>4</sub> and AgNO<sub>3</sub>). The total precursor concentration is 50 mM, containing X% AgNO<sub>3</sub> and (100-X)% CuSO<sub>4</sub>. The electrodeposition was conducted using a three-electrode setup with an Ag/AgCl (KCl sat.) reference electrode and Pt foil counter electrode. The electrodeposition was performed at 2 A cm<sup>-2</sup> for 1 min. Then, the electrode was instantly rinsed with DI-water to avoid galvanic replacement between Cu and Ag<sup>+</sup> and dried under air.

Oxide-derived Cu (OD-Cu) was synthesized from the electrooxidation, thermal treatment,<sup>2</sup> followed by a similar *in-situ* electroreduction as CuAg<sub>glv</sub>/Cu electrode. Specifically, the pre-cleaned Cu foams were first immersed in a one-compartment three-electrode cell with 3 M NaOH electrolyte as both the cathode and anode. Then, a constant current of 10 mA was applied to oxidize the surface of Cu foam to Cu(OH)<sub>2</sub> for 5 min, followed by cleaning in DI-water and drying in the oven. The dried Cu(OH)<sub>2</sub> was then placed into a ceramic boat and transferred to the tube furnace for heat treatment at 550 °C for 2 hours at a ramping rate of 3 °C min<sup>-1</sup> under Ar atmosphere. Finally, OD-Cu was obtained from *in-situ* electroreduction at the potential of  $-0.1$  V<sub>RHE</sub> for 3 min.

Ni<sub>2</sub>P electrode was prepared from a modified method in the literature.<sup>3</sup> Ni foam was first cleaned by 6 M HCl and DI-water for 15 min under sonication. Then, a 40 mL solution with 4 mmol NH<sub>4</sub>F, 10 mmol urea, and 4 mmol Ni(NO<sub>3</sub>)<sub>2</sub>·6H<sub>2</sub>O was prepared and transferred to a 50 mL Teflon-lined stainless steel autoclave. The hydrothermal growth of the hydroxides on Ni foam was performed at 120 °C for 6 hours with a heating rate of 3 °C min<sup>-1</sup>, followed by sonication in DI-water and drying in the oven at 80°C. Then, the as-synthesized hydroxides and 1.6 g of NaH<sub>2</sub>PO<sub>2</sub>·H<sub>2</sub>O powder were placed at two separate positions in a ceramic boat and transferred to a tube furnace. The NaH<sub>2</sub>PO<sub>2</sub>·H<sub>2</sub>O powder was placed at upstream of the Argon flow. After flushing by Ar for 30 min, the temperature was elevated to 300 °C at a ramping rate of 3 °C min<sup>-1</sup> and held at 300 °C for 2 hours under a static Ar atmosphere.

Cu nanoparticles (NPs)/Cu (1 mg<sub>catalyst</sub> cm<sup>-2</sup>) and Cu<sub>2</sub>O NPs/Cu (3 mg<sub>catalyst</sub> cm<sup>-2</sup>) were prepared by a spray-coating method on Cu foam substrate. Pt/C, IrO<sub>2</sub>, and RuO<sub>2</sub> (0.5 mg<sub>catalyst</sub> cm<sup>-2</sup>) were spray-coated on HNO<sub>3</sub>-treated carbon cloth substrates. The treatment of carbon cloth was conducted in 67–70 wt.% HNO<sub>3</sub> at 110°C for 1 h 45 min to improve its hydrophilicity. The catalyst ink was prepared by dispersing nanoparticles in a mixture of DI water and 2-propanol (10 mg<sub>Ag</sub> mL<sup>-1</sup>) with added ionomer by ultrasonication. The mass ratio of nanoparticles and ionomer was 4:1. The ink was then airbrushed onto the substrate to the final loadings.

### 3. CuO<sub>x</sub> reduction by aldehydes in the batch reactor

Autocatalytic CuO<sub>x</sub> reduction by aldehyde with H<sub>2</sub> production was carried out at room temperature in a gastight batch reactor for half hour. Specifically, 50 mg of Cu-based nanopowders was suspended in 15 mL of the solution with 200 mM furfural in 1 M KOH, and magnetically stirred at 350 r.p.m. by a PTFE-coated stir bar (20 × 6 mm). The solution was sparged with Ar during the test to carry the produced H<sub>2</sub> to the online gas chromatography (GC) for its quantification.

### 4. Electrochemical measurements in the H-type cell

To perform EOD reaction in an H-type cell, a three-electrode configuration was set up with Ag/AgCl as the reference electrode and Pt foil as the counter electrode. The resistance between the working and reference electrodes was determined by potentiostatic electrochemical impedance spectroscopy (PEIS), and 90% *IR*-compensation was applied for all electrochemical measurements. The geometric area of the working electrode was 1 cm<sup>2</sup>. Anode and cathode compartments were separated by a Nafion membrane (K<sup>+</sup> form). The electrolyte was prepared in 1 M KOH solution, and 15 ml of electrolyte was used in each compartment. It should be noted that the prepared furfural-containing electrolyte was conducted electrolysis instantly, in order to avoid its degradation to humins and minimize the side Cannizzaro reaction in the alkaline medium.

Linear sweep voltammetry (LSV) and chronoamperometry (CA) tests were conducted under a constant Ar flow through the catholyte for deaeration and online analysis of evolved H<sub>2</sub> by GC. LSV was carried out without magnetic stirring at 10 mV s<sup>-1</sup>. During CA tests, the catholyte and anolyte were stirred by PTFE-coated magnetic bars (20 × 6 mm, Chemglass Life Sciences) at 350 r.p.m. Potentials versus RHE relative to those versus Ag/AgCl was calculated by:

$$E_{\text{RHE}} = E_{\text{Ag/AgCl}} + 0.197 \text{ V} + 0.059 \text{ V} \times \text{pH}$$

### 5. Electrochemical measurements in the MEA-based flow electrolyzer

The flow electrolyzer contains two stainless steel flow-field plates with serpentine channels, PTFE and silicone gaskets, and the MEA, which contains two electrodes and a membrane, and

was formed after assembling the cell hardware. The catholyte and anolyte were circulated by a peristaltic pump (Masterflex<sup>®</sup> L/S<sup>®</sup>) at 10 ml min<sup>-1</sup>. To avoid the current density exceeding the limit of potentiostat, we applied custom-designed flow cell with active surface area of 1 cm<sup>2</sup> (1×1 cm<sup>2</sup>) for anode and 6.25 cm<sup>2</sup> (2.5× 2.5 cm<sup>2</sup>) for cathode. This cell configuration is based on the rate limiting step of the anodic EOD reaction in the EOD-HER paired system since HER is much favorable thermodynamically ( $E^0 = 0$  vs. SHE, at pH =0) and kinetically (on noble metal Pt/C catalysts). The applied potential or current was controlled by a Biologic SP-300 potentiostat/galvanostat with 70% *IR*-compensation. The membrane used to separate catholyte and anolyte was anion exchange membrane (Tokuyama A201) or dialysis membrane (Biotech CE Dialysis Trial Kit, MWCO of 0.1-0.5 kD, and thickness of 70 μm; Repligen Inc.). All experiments were performed at the room temperature.

## 6. Membrane characterization

### 6.1 Permeability

The permeability ( $P_s$ ) of 2-FA and furfuryl alcohol was determined using the same MEA-based flow cell set-up with a dialysis membrane or AEM to separate the anode and cathode. Anolyte and catholyte were circuited by 1 M KOH solution with and without 250 mM 2-FA or furfuryl alcohol, respectively. We then determined the 2-FA or furfuryl alcohol concentration in the catholyte at different time intervals. Subsequently, the permeability of certain chemicals was calculated based on their concentration changes over time using the equation as follows:

$$P_s = \frac{V_C}{c_A A} \frac{dc_C}{dt} = \frac{D_s}{L}$$

where  $V_C$  is the volume of the catholyte,  $L$  is the membrane thickness,  $A$  is the membrane area,  $t$  is time,  $D_s$  is their diffusion coefficient, and  $c_A$  and  $c_C$  are the concentration of alcohol or acid in anolyte and catholyte, respectively.

### 6.2 Calculation of conductivity and potential drops across the membrane

Since the dialysis membrane is a porous separator without any ion-selective preference across the membrane, sample molecules larger than the pores are retained on the sample-side of the membrane, while small ions would freely pass through the membrane. KOH in the electrolyte was dissociated into  $K^+$  and  $OH^-$  with equal charge; therefore, the overall conductance is given by the sum of their conductance as follows:

$$\Lambda = \lambda_i = \lambda_+ + \lambda_- = \frac{\kappa}{z_+ \nu_+ c} = \frac{\kappa}{c_{equiv}}$$

$\lambda_i$  is the equivalent ionic conductance, with the unit of S cm<sup>2</sup> equiv<sup>-1</sup>.  $\kappa$  is the conductivity with the unit of S m<sup>-1</sup>. The equivalent conductance for  $K^+$  and  $OH^-$  is 73.5 and 197.6 S cm<sup>2</sup> equiv<sup>-1</sup>, respectively.<sup>4</sup>

$$\Lambda = \lambda_+ + \lambda_- = 73.5 + 197.6 = \frac{\kappa}{c_{equiv}}$$

The concentration of 1 M is equal to 1/1000 equiv cm<sup>-3</sup>. Then, substituting into the above equation gives  $\kappa = 247$  mS cm<sup>-1</sup> for dialysis membrane.

The potential drop ( $\Delta\phi$ ) across the membrane is calculated as follows:

$$\Delta\phi = \frac{iL}{\kappa}$$

Where  $i$  is the current density (unit: A m<sup>-2</sup>) and  $L$  is the thickness of the membrane (unit: m). Therefore, for the dialysis membrane with a thickness of 70 μm and at 300 mA cm<sup>-2</sup>, the calculated  $\Delta\phi$  is 0.85 mV.

In comparison, based on the literature,<sup>5</sup> the  $\kappa$  value for AME (A201 membrane) is 15-20 mS cm<sup>-1</sup>. With its thickness of 28  $\mu\text{m}$  and at 300 mA cm<sup>-2</sup>, the calculated  $\Delta\phi$  is 5.6–4.2 mV.

### 6.3 Water uptake

The quantification of water uptake for membranes was modified from the literature.<sup>6</sup> The AEM or dialysis membrane was first stored in 1 M KCl for 24 hours at room temperature. Then, the cleaned membrane was transferred to DI water for additional 24-hour storage at room temperature. Finally, the membrane was soaked in 1 M KOH for 1 hour. After gently removing the surface water by paper tissues, the mass of each hydrated membrane ( $m_h$ , g) was immediately measured by an analytical balance. For another 24-hour drying in the atmosphere, the mass of each dried membrane ( $m_d$ , g) was tested. The water uptake value can be calculated from the equation as follow:

$$WU(\%) = \frac{m_h - m_d}{m_d} \times 100\%$$

### 7. Product analysis

The electrolyte was analyzed by High-Performance Liquid Chromatography (HPLC, Agilent Technologies, 1260 Infinity II LC System) equipped with a variable wavelength detector (Agilent 1260 Infinity Variable Wavelength Detector VL). The column (Bio-Rad Aminex HPX-87H) for analyzing anodic species (including furfural and 2-FA) was operated at 50 °C with a mobile phase of 0.01 M H<sub>2</sub>SO<sub>4</sub> at 0.5 ml min<sup>-1</sup>, and the wavelength of 260 nm was applied. For the quantification of furfuryl alcohol that produced from Cannizzaro reaction, a C18 HPLC column (Gemini® 3  $\mu\text{m}$ , 110 Å, 100 × 3 mm) was used at 45 °C with a binary gradient pumping method to drive mobile phase containing water and CH<sub>3</sub>CN at 0.4 ml min<sup>-1</sup> with the wavelength of 225 nm. The CH<sub>3</sub>CN fraction was increased from an initial volumetric ratio of 15% to 60% during 5–15 min, and then was decreased to 15% from 17–24 min.

H<sub>2</sub> was quantified by on-line GC (SRI Instrument 8610C MG#3) equipped with HaySep D and MolSieve 5 Å columns and a thermal conductivity detector. The calibration curve was established by analyzing the standard calibration gases with different concentrations (10–10,000 ppm).

The GC program was started 2 min after the electrolysis was initiated, and a 4.5-min programmed cycle (including a 4-min running period and a 0.5-min cooling period) was repeated throughout the measurement.

The rate of H<sub>2</sub> generation ( $r$ , mol s<sup>-1</sup>) for each cycle was calculated by the following equation:

$$r = c \times 10^{-6} \times [P\dot{V} \times 10^{-6}/(RT)]$$

Where  $c$  is the H<sub>2</sub> concentration (ppm);  $\dot{V}$  is the volumetric flow rate of the inlet gas (12.5 ml min<sup>-1</sup>);  $p$  is the ambient pressure ( $p = 1.013 \times 10^5$  Pa);  $R$  is the gas constant ( $R = 8.314$  J mol<sup>-1</sup> K<sup>-1</sup>);  $T$  is the room temperature (293.15 K). The total amount of H<sub>2</sub> (mol) was calculated by integrating the plot of H<sub>2</sub> production rate (mol s<sup>-1</sup>) vs. reaction time (s) with polynomial curve fitting.

The Faradaic efficiency (FE<sub>*i*</sub>) and partial current density of H<sub>2</sub> ( $j_{H_2}$ ) can be calculated by equations as follows:

$$FE_i = \frac{n_i z_i F}{Q} \times 100 \%$$

$$j_{H_2} = \frac{Q}{t} \times FE$$

Where  $n_0$  is initial moles of reactant;  $n$  is the moles of reactant after electrolysis;  $n_i$  is the moles of product  $i$ ;  $z_i$  is the number of electrons transferred for one product molecule;  $F$  is the Faraday constant ( $96,485 \text{ C mol}^{-1}$ );  $Q$  is the total charge passed through the electrolytic cell;  $t$  is the electrolysis time (s). In particular, the produced 2-FA from the EOD pathway is calculated by subtracting 2-FA that was generated from the Carnizarro pathway (by quantifying furfuryl alcohol) from the total detected 2-FA.

The identification of geminal diols from aldehydes in alkaline media was obtained from  $^1\text{H}$  NMR spectroscopy via a Bruker 600 MHz NMR spectrometer (AVIII-600). The samples were prepared by mixing 100 mM furfural-containing electrolyte with different concentrations of KOH with  $\text{D}_2\text{O}$  in a volume ratio of 9:1. NMR analysis was conducted using a WATERGATE method for background water peak suppression. The ratio of diols was directly quantified by comparing the H peak in the aldehyde group with other H peaks in the furan rings, and with the H peaks in standard furfural samples without base.

## 8. Materials characterization

### 8.1 Physical characterization

X-ray diffraction (XRD) crystallography was carried out on a Siemens D500 X-ray diffractometer with a Cu  $K\alpha$  source ( $\lambda = 1.5418 \text{ \AA}$ ) at a tube voltage of 45 kV and a tube current of 30 Ma. The scan was performed at a rate of  $10^\circ \text{ min}^{-1}$  and a step size of  $0.01^\circ$ . X-ray photoelectron spectroscopy (XPS) was carried out on a Kratos Amicus/ESCA 3400 X-ray photoelectron spectrometer with Mg  $K\alpha$  X-ray ( $1,253.7 \text{ eV}$ ). All spectra were calibrated with the C 1s peak at  $284.8 \text{ eV}$ . Scanning Electron Microscopy-Energy Dispersive X-ray Spectroscopy (SEM-EDS) was performed on a field-emission scanning electron microscope (FEI Quanta-250) equipped with a light-element X-ray detector and an Oxford Aztec energy-dispersive X-ray analysis system. Inductively coupled plasma-optical emission spectroscopy (ICP-OES) was performed on a PerkinElmer<sup>®</sup> Optima<sup>™</sup> 8000 ICP-OES instrument. Inductively coupled plasma mass spectrometry (ICP-MS) was performed from an Agilent 7700X instrument. Transmission electron microscopy (TEM) samples were prepared by scratching the nanopowders from the CuAg/Cu foam surface. The scratched material was dispersed in ethanol and ultrasonicated for 5 min, followed by drop-casting on the grid. Aberration corrected scanning transmission electron microscopy (STEM) images and energy-dispersive X-ray spectroscopy (EDS) mappings were taken from a Titan Themis 300 probe corrected TEM with a Super-X EDS detector. All Cu-based samples were temporarily stored under inter gas before characterizations, in order to avoid their possible oxidation in air.

### 8.2 Determination of the roughness factor

Surface roughness factors for the electrodes relative to copper foam were determined by measuring double-layer capacitances ( $C_{dl}$ ). Cyclic voltammetry (CV) was performed in a one-compartment electrochemical cell with 1 M KOH solution in a three-electrode configuration without stirring. The potential range for CV was conducted in the potential regions where no faradaic processes occurred, and the geometric current density difference ( $\Delta j$ ) was plotted against different scan rates of CV ( $20$  to  $200 \text{ mV s}^{-1}$ ).

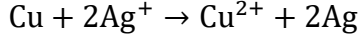
## 9. Calculation of Nernstian equilibrium shift

Nernst equation can be expressed as follow:

$$E = E^\circ + \frac{RT}{nF} \ln \frac{a_{ox}}{a_{red}}$$

Where  $E^\circ$  is the standard potential for the full cell at 25 °C,  $E$  is the actual full cell potential,  $R$  is the ideal gas constant,  $T$  is the temperature,  $n$  is the number of transferred electrons,  $F$  is the Faraday constant,  $a_{ox}$  is the activity of the oxidized species, and  $a_{red}$  is the activity of the reduced species.

To prepare the CuAg<sub>glv</sub>/Cu from galvanic replacement method, the following reaction occurs:



When the concentration of the precursor  $\text{Ag}^+$  varied from 1 mM to 200 mM, the Nernstian shift of the equilibrium potential equals:

$$\Delta E = \frac{0.059}{2} [\log(0.2^2) - \log(0.001^2)] = 0.14 \text{ V}$$

Thus, varying the concentration of  $\text{Ag}^+$  provided a tunable driving force to etch the Cu surface and create different relative abundance of  $\text{Cu}_2\text{O}$ .

## 10. DFT calculations

DFT calculations were performed within the Vienna Ab initio simulation package (VASP, version 5.4.4), using the periodic supercell approach. The projector augmented wave (PAW) method was used for describing electron-ion interactions.<sup>7, 8</sup> The Perdew-Burke-Ernzerhof functional with dispersion correction (PBE-D3) described the electron-electron exchange and correlation energies.<sup>9</sup> PBE-D3 has been shown earlier to describe furfural oxidation mechanistic trends consistent with experiment.<sup>10-13</sup> A plane wave basis set was used with an energy cutoff of 450 eV. For geometry optimizations, the convergence criteria of the forces acting on atoms was 0.05 eV Å<sup>-1</sup>, while the energy threshold defining self-consistency of the electron density was 10<sup>-5</sup> eV. Climbing image nudged elastic band (CI – NEB) method was used to search for the transition state structures. The structure of a transition state was considered converged with the atomic forces meeting the same 0.05 eV Å<sup>-1</sup> force convergence, and a single imaginary vibrational mode along the reaction coordinate.

**Model:** a cubic cell of 15×15×15 Å<sup>3</sup> was used for calculating the energetics of isolated molecules. The Pt/Cu/Au (111) metal slabs were constructed with a 3×3 unit cell composed of five atomic layers. The bottom three layers of the slab were constrained at their bulk lattice positions, with a lattice constant 3.976/3.592/4.078 Å determined as optimal with DFT calculations of the bulk structure. A vacuum region of 15 Å, before adding adsorbates, was used between the periodic slabs in the surface normal direction to minimize the interactions between periodic slabs. Slab-to-slab dipole interactions were corrected using the VASP keywords (LDIPOL = TRUE, IDIPOL = 3).

**Elementary electrochemical reaction energies:** The geometries of all surface bound intermediates were fully optimized, considering multiple initial adsorption configurations to determine the lowest energy structures. The geometries of all fully optimized intermediates are illustrated below in **Fig. S7**.

The free energy of each adsorbed intermediate was calculated as:

$$G_{int}^* = E_{int}^* + E_{ZPVE} + E_{vib} - TS_{vib} \quad (1)$$

where,  $E_{int}^*$  is the DFT optimized energy of the adsorbed intermediate,  $E_{ZPVE}$  is the zero-point vibrational energy,  $E_{vib}$  is the internal energy stored in vibration at 300 K, and  $TS_{vib}$

represents the vibrational entropy of the adsorbed species at 300 K.  $E_{vib}$  and  $TS_{vib}$  are calculated using standard ab-initio thermodynamic approaches. Free energies of gas phase species were calculated by including PV, translational, rotational, and vibrational energy and entropy terms, treating each species as an ideal gas. The free energy of water was calculated at 0.03 atm, the vapor pressure of water at atmospheric conditions, whereas all other gas phase chemical potentials were determined at 1 atm. Reaction energies per mole of reactant consumed were calculated according to stoichiometric balance of reactants, products, as defined in **Scheme 1 and Table S3-4**. Reaction free energies for non-electrochemical reactions are calculated simply as the free energy of reactants subtracted from the products. For electrochemical reactions, the free energy of the proton-electron pair is determined using computational hydrogen electrode approach whereas the free energy of the proton-electron pair is estimated using the free energy of H<sub>2</sub> gas at 1 bar and the linear dependence of the electron energy on electrode potential.<sup>14</sup>

**Potential-dependent activation barriers:** Activation barriers for elementary electrochemical oxidation steps were calculated as a function of electrode potential ( $U$ ) based on a local model of electrochemical reaction with a simple procedure outlined in previous work.<sup>15, 16</sup> This method approximates activation barriers of an electrochemical oxidation steps in water electrolyte (deprotonation and hydroxylation or oxygen addition) by calculating the transition state for an equivalent A-H breaking or A-OH formation step, then assigns the calculated barrier  $E_{act}^0(U^0)$  to the potential defined as  $U^0$  at which the H or OH species in the unit cell has the same chemical potential as the water, protons, and electrons involved in generating it. C-H bond breaking in this study is considered a non-electrochemical Tafel like step while O-H bond cleavage is considered a single electron transfer step as established in previous studies. We calculate  $U^0$  for reactions of the form  $A^* + H_2O \rightarrow (A-OH)^* + H^+ + e^-$  using Eq. (2). The corresponding activation barriers " $E_{act}^0(U^0)$ " are calculated using addition of a surface hydroxyl to the surface adsorbate.

$$U^0 = \frac{G_{(A^*+OH^*)} + \frac{1}{2}G_{H_2} - G_{A^*} - G_{H_2O}}{e} \quad (2)$$

The potential dependent activation barrier is determined using the Butler-Volmer extrapolation as shown in Eq. (3) assuming a known value of  $\beta$ .

$$E_{act}(U) = E_{act}^0(U^0) - \beta e(U - U^0) \quad (3)$$

$\beta$  is a reaction symmetry factor denoting the relationship between the activation barrier and reaction energy change.<sup>17</sup>  $\beta$  is typically between 0.3 and 0.7 based on experimental observations and theoretical calculations.<sup>18</sup> Here, we approximate  $\beta$  equal to 0.5 for all one electron steps; varying values within physical ranges for different steps has little influence on catalytic trends. The barrier is taken to have reached 0 when Eq. (3) produces a negative barrier. The most stable geometries of key intermediates and transition states are shown in **Fig. S7**. Reaction energies and activation barriers of the key elementary steps is reported in **Table S3**.

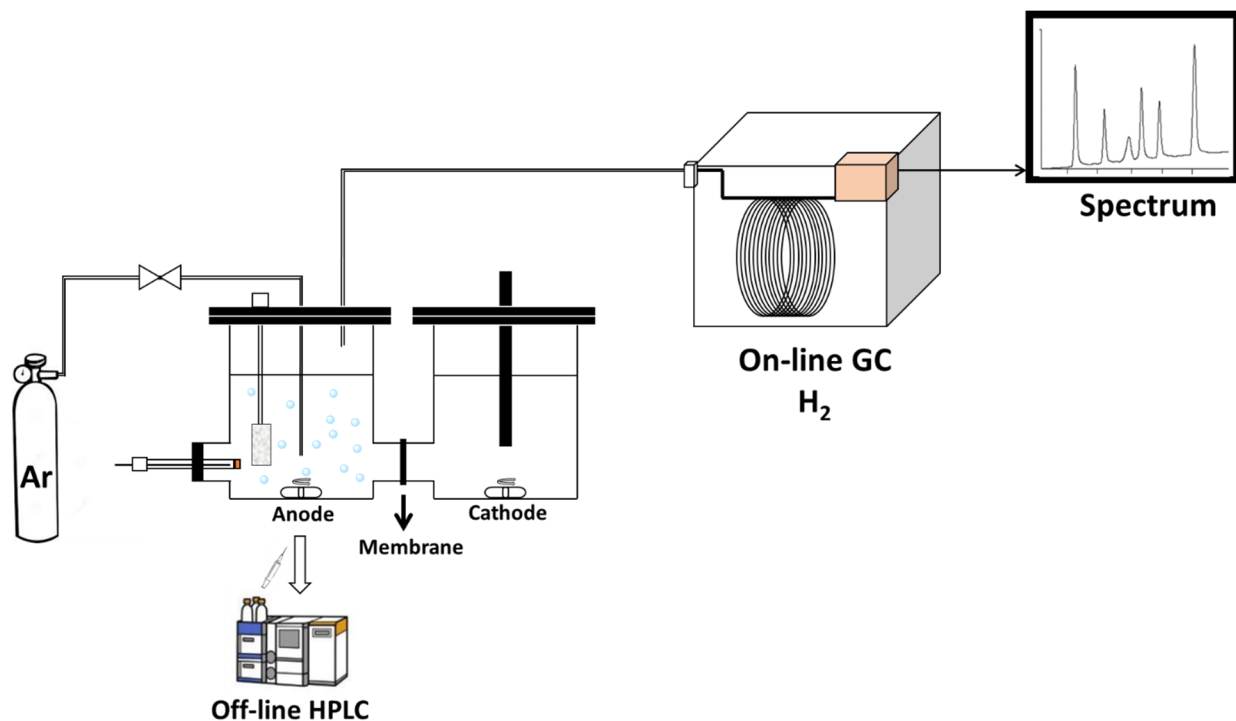


**Fig. S1** The experimental setup for EOD of furfural, including the H-type cell for electrochemical tests, on-line GC for H<sub>2</sub> quantification, and HPLC for off-line quantification of furfuryl alcohol, 2-FA and furfural.

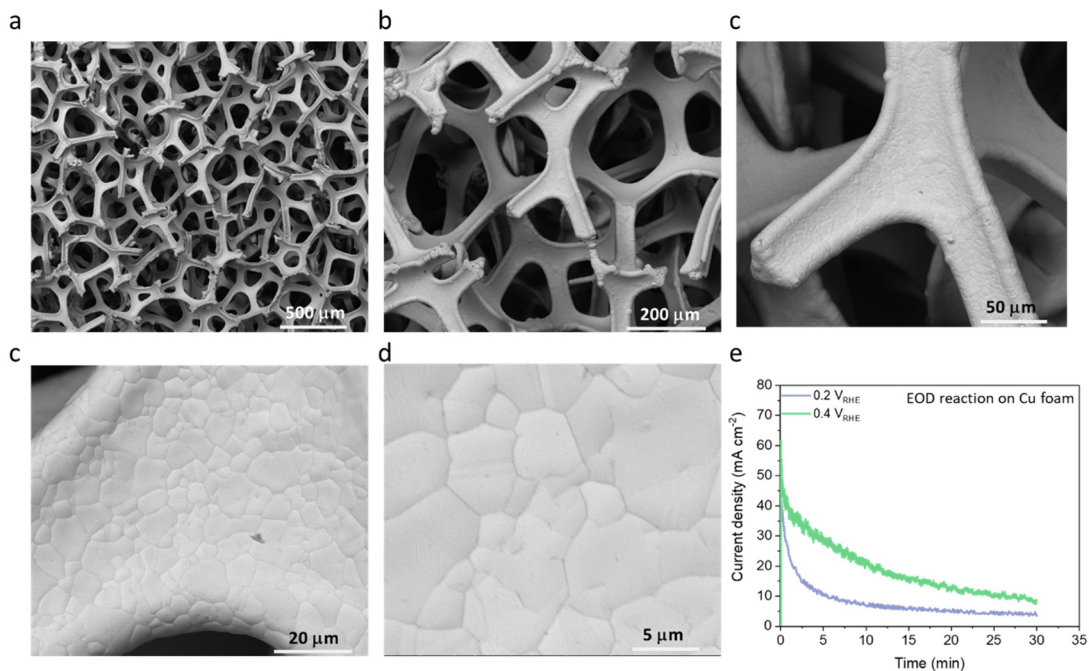


**Fig. S2** (a)-(d) SEM images of plain Cu foam. (e) Current density – time profiles on pre-cleaned Cu foam at different potentials for half-hour EOD electrolysis.

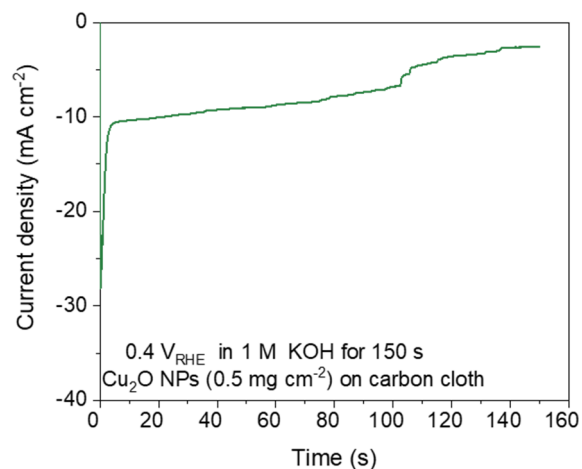


**Fig. S3** Current density – time profile of  $\text{Cu}_2\text{O}$  nanoparticles on carbon cloth. The electrolysis was performed at  $0.4 V_{\text{RHE}}$  in 1 M KOH solution.

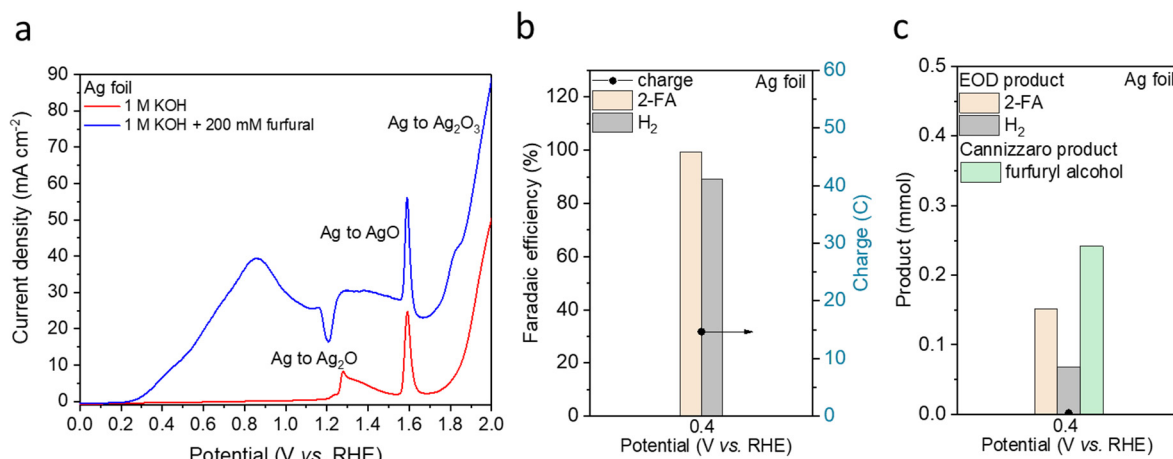


**Fig. S4** EOD reaction on Ag foil. (a) LSV (2<sup>nd</sup> cycle) on Ag foil ( $1\text{cm}^2$ ) with or without 200 mM furfural in 1 M KOH electrolyte. (b) Faradaic efficiency (left y-axis) and passed charge (right y-axis), and (c) detected products for half-hour electrolysis in 1 M KOH with 200 mM furfural at  $0.4 V_{\text{RHE}}$ .

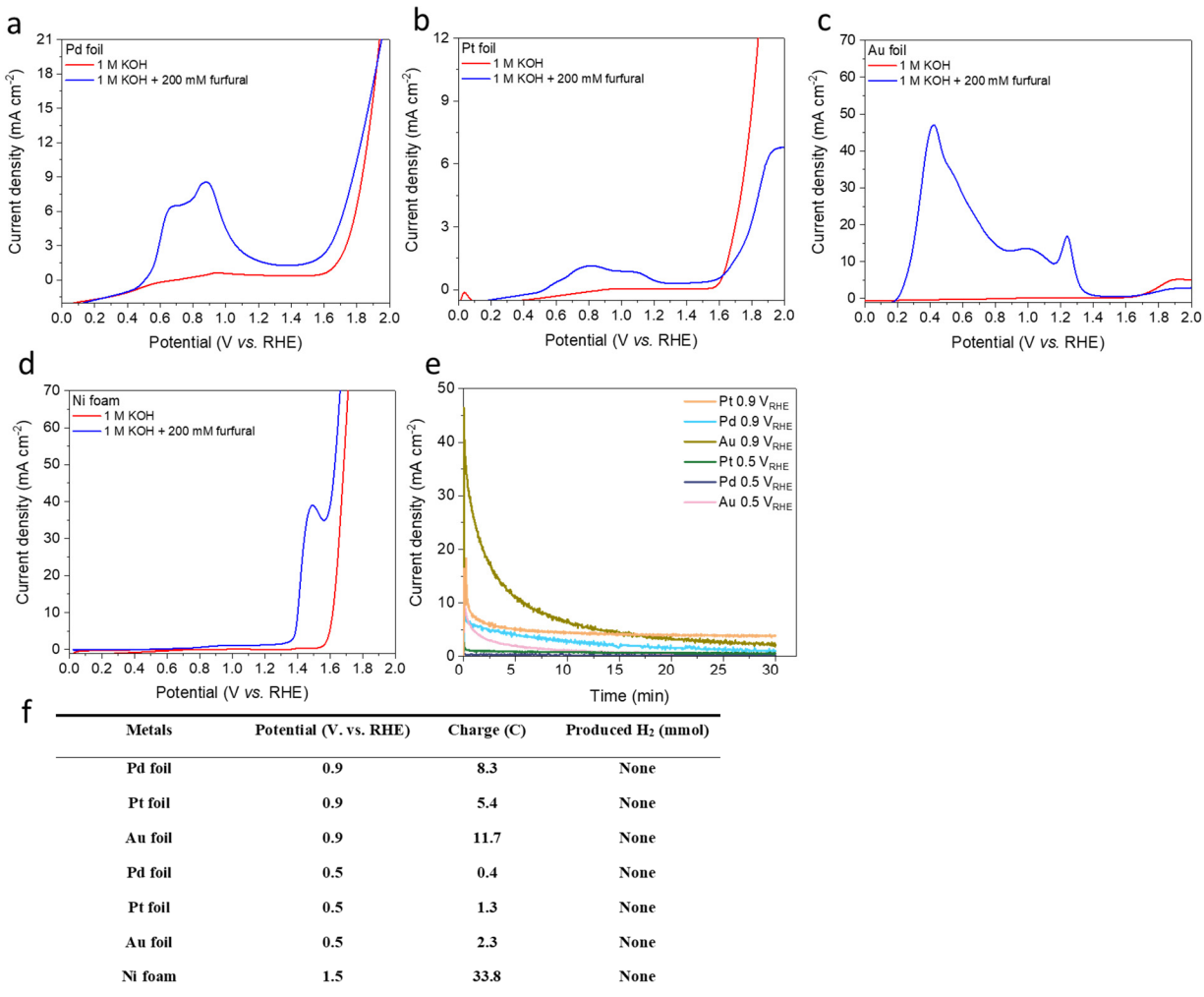


**Fig. S5 EOD reaction on different metal foils/foams.** LSV (2<sup>nd</sup> cycle) on (a) Pd foil, (b) Pt foil, (c) Au foil, and (d) Ni foam with or without 200 mM furfural in 1 M KOH electrolyte. (e) Current density – time profiles at different electrodes with different potentials. (f) Summary of the charge and produced H<sub>2</sub> for half-hour electrolysis on different metals.

**Table S1. Cannizzaro reactions on different nanoparticles.<sup>a</sup>**

Conditions	Produced 2-FA by Cannizzaro reaction (mmol)
No catalyst	0.27
Ag foil (1 cm <sup>2</sup> )	0.30
50 mg Cu NPs	0.72
50 mg Ag NPs	0.67

a. Cannizzaro reactions were conducted in the batch reactor stirred at 350 r.p.m for a half hour. 200 mM furfural was dissolved in 15 mL of 1 M KOH as the reaction solution.

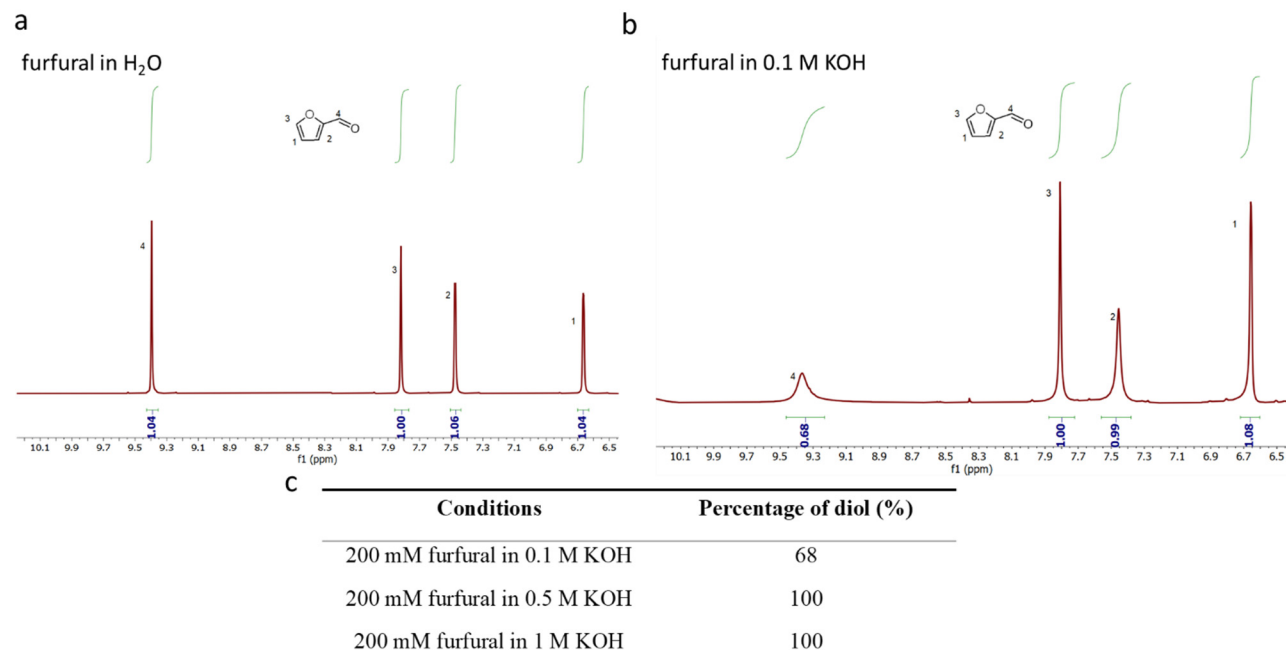


**Fig. S6 NMR for identification and quantification of diols at different base solutions.** <sup>1</sup>H NMR (600 MHz, H<sub>2</sub>O+D<sub>2</sub>O) δ 9.40 (s, 1H), 7.82 (s, 1H), 7.48 (d, *J* = 3.7 Hz, 1H), 6.66 (dd, *J* = 3.9, 1.9 Hz, 1H).

**Table S2.** DFT calculated binding energies of key surface moieties on Pt/Cu/Au (111) surfaces. Binding energies were calculated as the reaction free energy for forming the reactive surface moieties from their corresponding stable counterparts as shown below.

Species	Corresponding reaction	Binding Energies (eV)		
		Pt	Cu	Au
<b>H*</b>	$0.5 \text{ H}_2(\text{g}) + * \rightarrow \text{H}^*$	-0.53	0.31	0.38
<b>OH*</b>	$\text{H}_2\text{O}(\text{l}) + * \rightarrow \text{OH}^* + 0.5 \text{ H}_2$	0.58	0.51	1.33
<b>CO*</b>	$\text{CO}(\text{g}) + * \rightarrow \text{CO}^*$	-1.63	-0.63	0.15
<b>FCHO*</b>	$\text{FCHO}(\text{g}) + * \rightarrow \text{FCHO}^*$	-2.11	-1.06	-0.96
<b>FCOOH*</b>	$\text{FCOOH}(\text{g}) + * \rightarrow \text{FCOOH}^*$	-2.09	-1.12	-1.01

**Table S3.** Reaction energetics of key elementary steps for EOD reaction using Carbonyl or Diol route.

Furoic acid formation pathways		$\Delta G_{\text{rxn}}$ (eV)	$E_a^0$ (eV)	$U^0$ (V)
<b>Carbonyl route</b>	$\text{R-CHO}^* + * \rightarrow \text{R-CO}^* + \text{H}^*$	0.45	0.72	NA
	$\text{R-CO}^* + \text{H}_2\text{O} \rightarrow \text{R-COOH}^* + \text{H}^+ + \text{e}^-$	-0.81	0.45	0.48
<b>Diol route</b>	$\text{R-CH}(\text{OH})_2(\text{g}) + * \rightarrow \text{R-CHO}(\text{OH})^* + \text{H}^+ + \text{e}^-$	-0.32	0	NA
	$\text{R-CHO}(\text{OH})^* + * \rightarrow \text{R-COOH}^* + \text{H}^*$	-0.87	0.35	NA

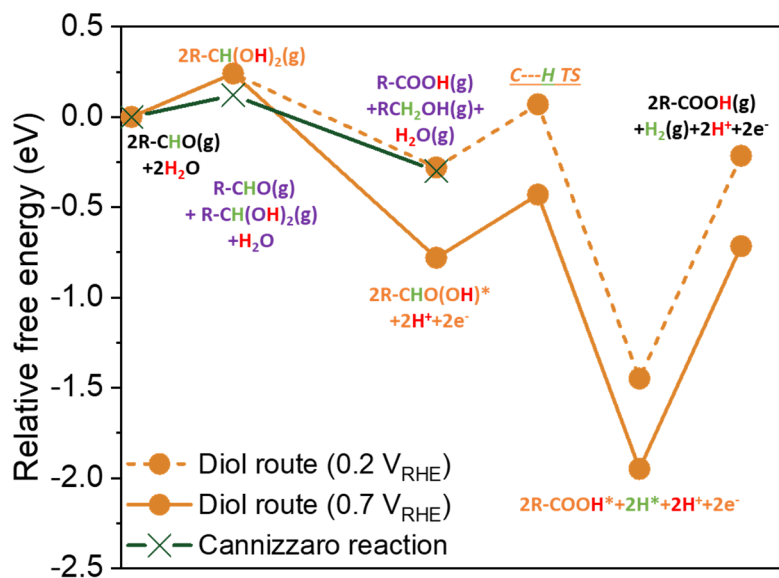


**Fig. S7** Reaction free energy diagram for the diol-mediated EOD reaction path (at 0.2 V<sub>RHE</sub> and 0.7 V<sub>RHE</sub>, on the Cu(111) surface) and the Cannizzaro reaction. The diol-mediated EOD reaction becomes more energetically favorable relative to the Cannizzaro reaction at the more oxidizing potential. The inset shows the RCHO(OH)\* optimized structure and the transition state structure for the C-H activation step for the adsorbed diol.

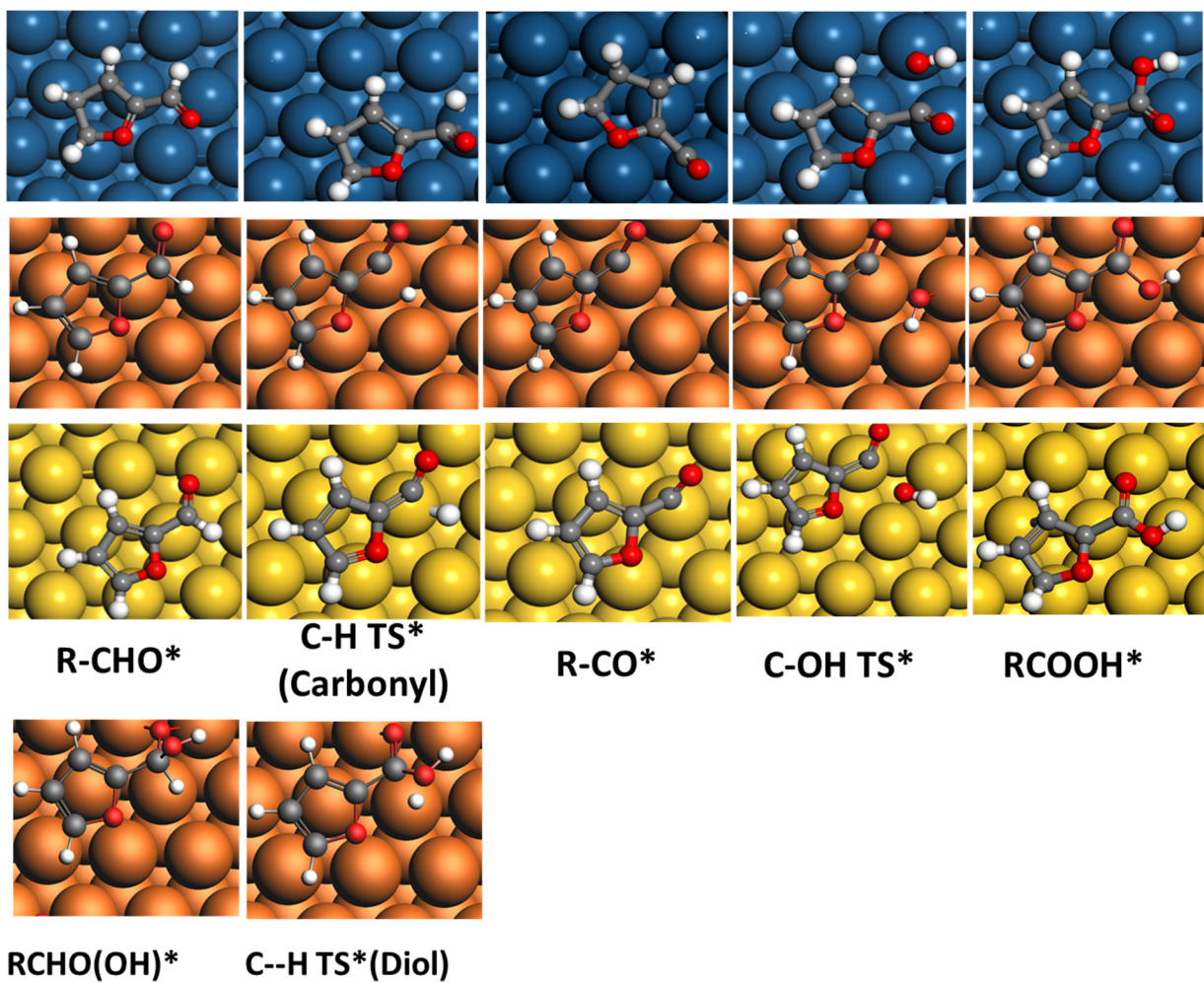


**Fig. S8** Optimized geometries of key intermediates of EOD reactions. Rows (1-3) show structures along the carbonyl route on Pt/Cu/Au (111) surfaces. Row 4 shows structures along the diol route on the Cu (111) surface.

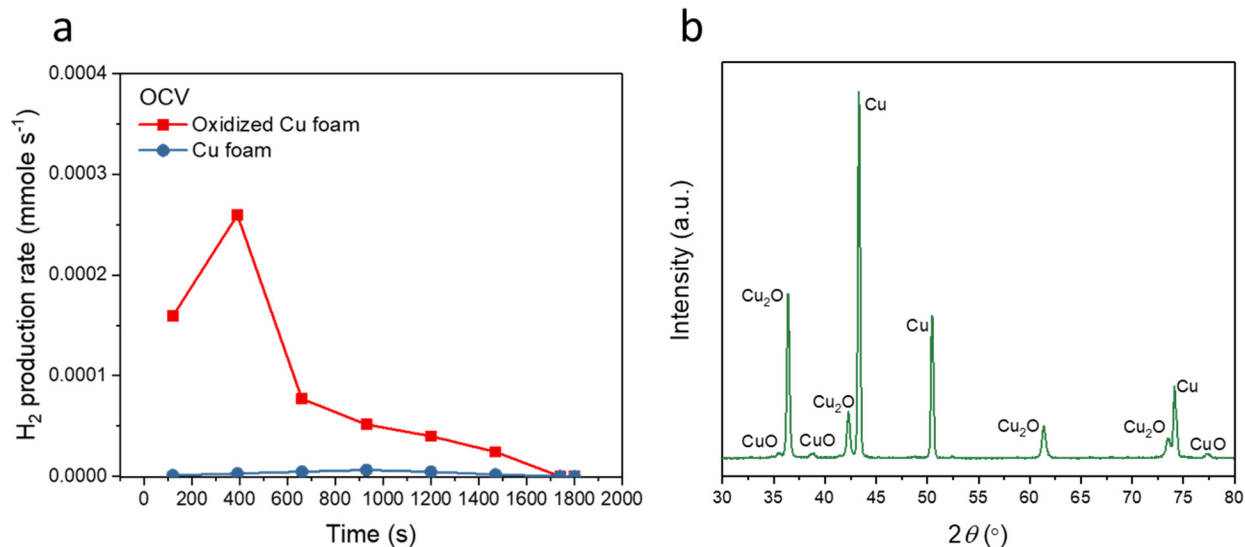


**Fig. S9 CuO<sub>x</sub> reduction by aldehydes with H<sub>2</sub> evolution on Cu-based electrodes (1 cm<sup>2</sup>) under OCV.** (a) H<sub>2</sub> production rate. (b) XRD pattern of oxidized Cu foam. We found that unlike the hysteresis behavior of H<sub>2</sub> evolution on copper oxides powders (**Fig. S10**), H<sub>2</sub> was instantly evolved when the oxidized Cu foam was in contact with the furfural-containing solution, which suggested a much more efficient electron transfer. This is because of the direct electrical contact between copper and copper oxides (similar to a heterojunction) that largely avoided a diffusion-controlled reduction of Cu oxides to Cu as seeds at the early stage of the reaction.

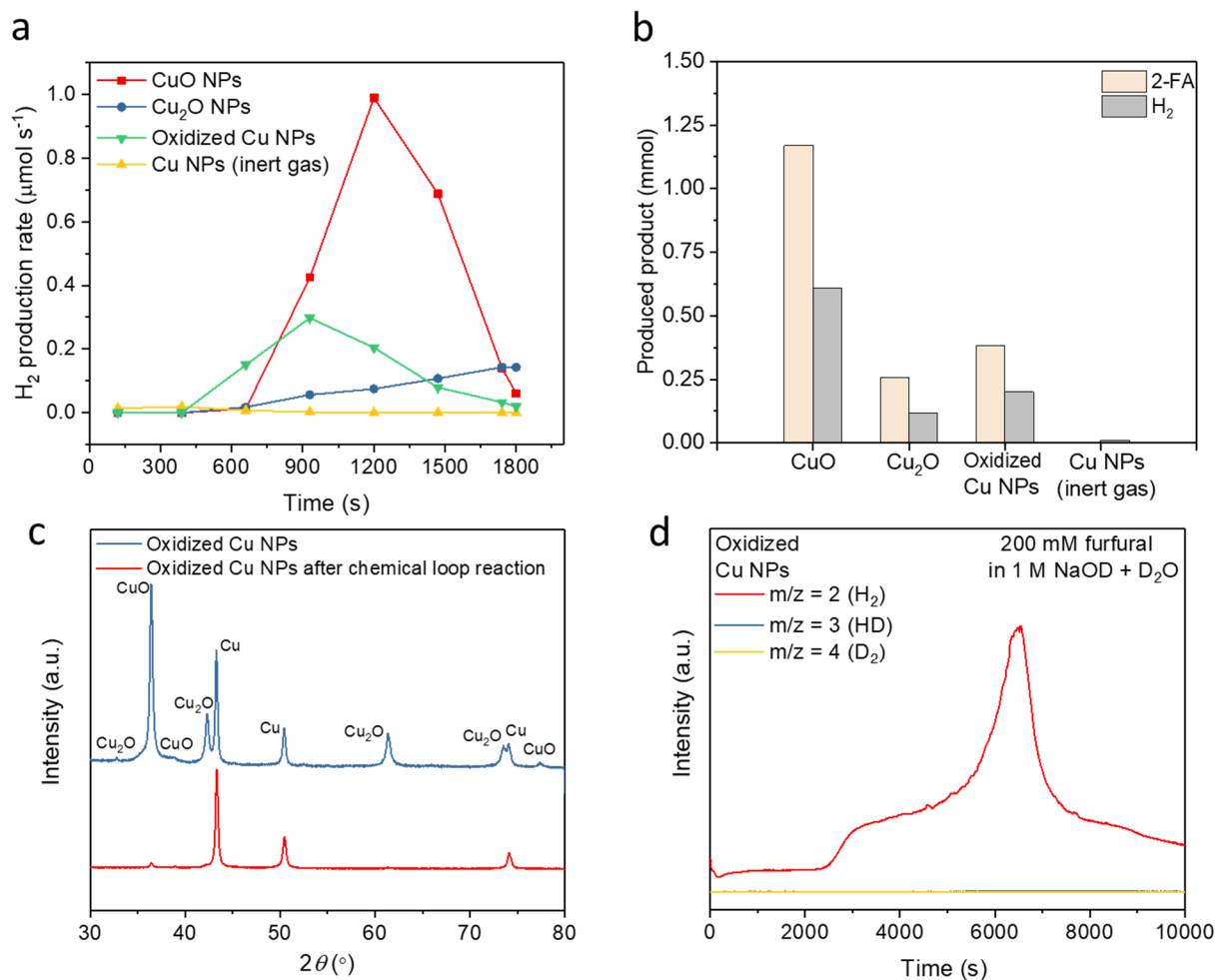


**Fig. S10 CuO<sub>x</sub> (50 mg) reduction by aldehydes with H<sub>2</sub> evolution.** (a) H<sub>2</sub> production rate and (b) product on various Cu-based nanoparticles for half-hour reaction. To avoid the oxidation of Cu NPs by air, the catalyst preparation was operated under inert gas in the glove box. (c) XRD patterns of oxidized Cu NPs before and after the reaction. The XRD intensity was normalized to Cu(111) peak at ~43.3°. These reactions were conducted in 1 M KOH with 200 mM furfural. (d) DEMS signals for the reaction on oxidized Cu NPs in the solution with 200 mM furfural in 1 M NaOD and D<sub>2</sub>O.

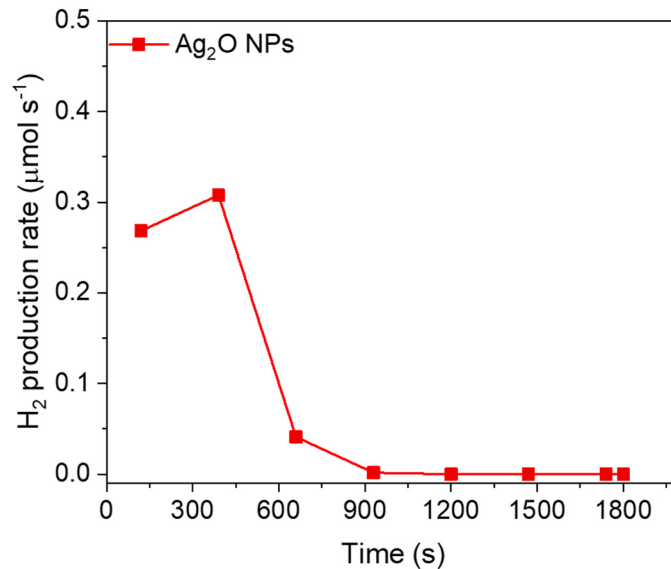


**Fig. S11 Ag<sub>2</sub>O (50 mg) reduction by aldehydes with H<sub>2</sub> evolution.** The H<sub>2</sub> evolution reaction was conducted in 1 M KOH with 200 mM furfural. We noticed that H<sub>2</sub> instantly evolved after adding Ag<sub>2</sub>O to the solution, and its full evolution took shorter time than that on CuO<sub>x</sub>, likely due to the more favorable thermodynamics of Ag<sub>2</sub>O reduction in the presence of aldehyde (**Table S5**).

## Supplementary note 1, thermodynamic analysis

The calculation of the equilibrium potentials for different reactions mentioned in the main text was shown by the equation as follows:

$$\Delta G = -nFE^\circ$$

where  $\Delta G$  is the Gibbs free energy of reaction at 298 K and 1 bar,  $F$  is Faraday's constant, and  $n$  is the number of electrons passed during the reaction. All thermodynamic data is from NIST webbook or the electrochemical textbook.<sup>4</sup> It should be noted that because the lacking of thermodynamic data of furfural from database and literature, we used HCHO for thermodynamic analysis. This reactant also exhibited EOD activity with similar performance as furfural from our experimental data.

**Table S4.** Thermodynamic data of different substances.

Substance	$\Delta H_f^\circ$ (kJ mol <sup>-1</sup> )	$S^\circ, 1 \text{ bar}$ (J mol <sup>-1</sup> K <sup>-1</sup> )	$\Delta G$ (298.15 K, 1 bar)
Cu			0
CuO			-129.70
OH <sup>-</sup>	-229.99	-10.54	-226.85
H <sub>2</sub> O	-285.83	69.95	-306.69
Ag			0
HCHO	-115.9	218.95	-181.18
HCOOH	-425.09	131.84	-464.40

**Table S5.** Thermodynamic data of different reactions.

Reaction	Reaction question	$\Delta G$ (298.15 K, 1 bar)	$E^0$ (vs. NHE, at pH = 0)
Cathode	$\text{CuO} + 2\text{e}^- + \text{H}_2\text{O} \rightarrow \text{Cu} + 2\text{OH}^-$	52.40	-0.27
	$\text{Cu}_2\text{O} + 2\text{e}^- + \text{H}_2\text{O} \rightarrow 2\text{Cu} + 2\text{OH}^-$	69.47	-0.36
	$\text{Ag}_2\text{O} + 2\text{e}^- + \text{H}_2\text{O} \rightarrow 2\text{Ag} + 2\text{OH}^-$	-66.00	0.34
	$\text{Pd}^{2+} + 2\text{e}^- \rightarrow \text{Pd}$	-183.32	0.95
	$\text{Pt}^{2+} + 2\text{e}^- \rightarrow \text{Pt}$	-227.70	1.18
Anode	$2\text{H}_2\text{O} + 2\text{e}^- \rightarrow \text{H}_2 + 2\text{OH}^-$	159.68	-0.83
	$2\text{HCHO} + 4\text{OH}^- \rightarrow 2\text{HCOO}^- + 2\text{H}_2\text{O} + \text{H}_2 + 2\text{e}^-$	-272.42	1.41
	$\text{HCHO} + 3\text{OH}^- \rightarrow \text{HCOO}^- + 2\text{H}_2\text{O} + 2\text{e}^-$	-216.05	1.12
	$\text{CuO} + 2\text{HCHO} + 2\text{OH}^- \rightarrow \text{Cu} + \text{H}_2\text{O} + \text{H}_2 + 2\text{HCOO}^-$	-359.44	1.86
Combined	$\text{Cu}_2\text{O} + 2\text{HCHO} + 2\text{OH}^- \rightarrow 2\text{Cu} + \text{H}_2\text{O} + \text{H}_2 + 2\text{HCOO}^-$	-290.89	1.51
	$\text{Ag}_2\text{O} + 2\text{HCHO} + 2\text{OH}^- \rightarrow 2\text{Ag} + \text{H}_2\text{O} + \text{H}_2 + 2\text{HCOO}^-$	-503.30	2.61
	$\text{Pd}^{2+} + 2\text{HCHO} + 4\text{OH}^- \rightarrow 2\text{HCOO}^- + \text{Pd} + 2\text{H}_2\text{O} + \text{H}_2$	-595.16	3.08
	$\text{Pt}^{2+} + 2\text{HCHO} + 4\text{OH}^- \rightarrow 2\text{HCOO}^- + \text{Pt} + 2\text{H}_2\text{O} + \text{H}_2$	-639.54	3.31
	$\text{HCHO} + \text{OH}^- \rightarrow \text{HCOO}^- + \text{H}_2$	-126.02	0.65

**Table S6.** Summary of different cathodic half-reactions as electron-scavengers.

Reaction	Types	Cathode	Anode	Overall
$\text{CuO}_x$ reduction	galvanic cell	$\text{CuO}_x + 2\text{x e}^- + \text{xH}_2\text{O} \rightarrow \text{Cu} + 2\text{xOH}^-$	outer-sphere (catalyst independent)	$\text{CuO}_x + 2\text{RCHO} + 2(2-\text{x})\text{OH}^- + 2(\text{x}-1)\text{e}^- \rightarrow \text{Cu} + 2\text{RCOO}^- + (2-\text{x})\text{H}_2\text{O} + \text{H}_2$
EOD-HER	electrolytic cell	$2\text{H}_2\text{O} + 2\text{e}^- \rightarrow 2\text{OH}^- + \text{H}_2$	inner-sphere (catalyst dependent) $2\text{RCHO} + 4\text{OH}^- \rightarrow 2\text{RCOO}^- + 2\text{H}_2\text{O} + \text{H}_2 + 2\text{e}^-$	inner-sphere (catalyst dependent) $\text{RCHO} + \text{OH}^- \rightarrow \text{RCOO}^- + \text{H}_2$
EOD-ORR <sup>a</sup>	galvanic cell	$\text{O}_2 + 2\text{H}_2\text{O} + 4\text{e}^- \rightarrow 4\text{OH}^-$	inner-sphere (catalyst dependent)	$4\text{RCHO} + \text{O}_2 + 4\text{OH}^- \rightarrow 4\text{RCOO}^- + 2\text{H}_2 + 2\text{H}_2\text{O}$

[a]. The system of EOD-ORR is adapted from literature<sup>19</sup>.

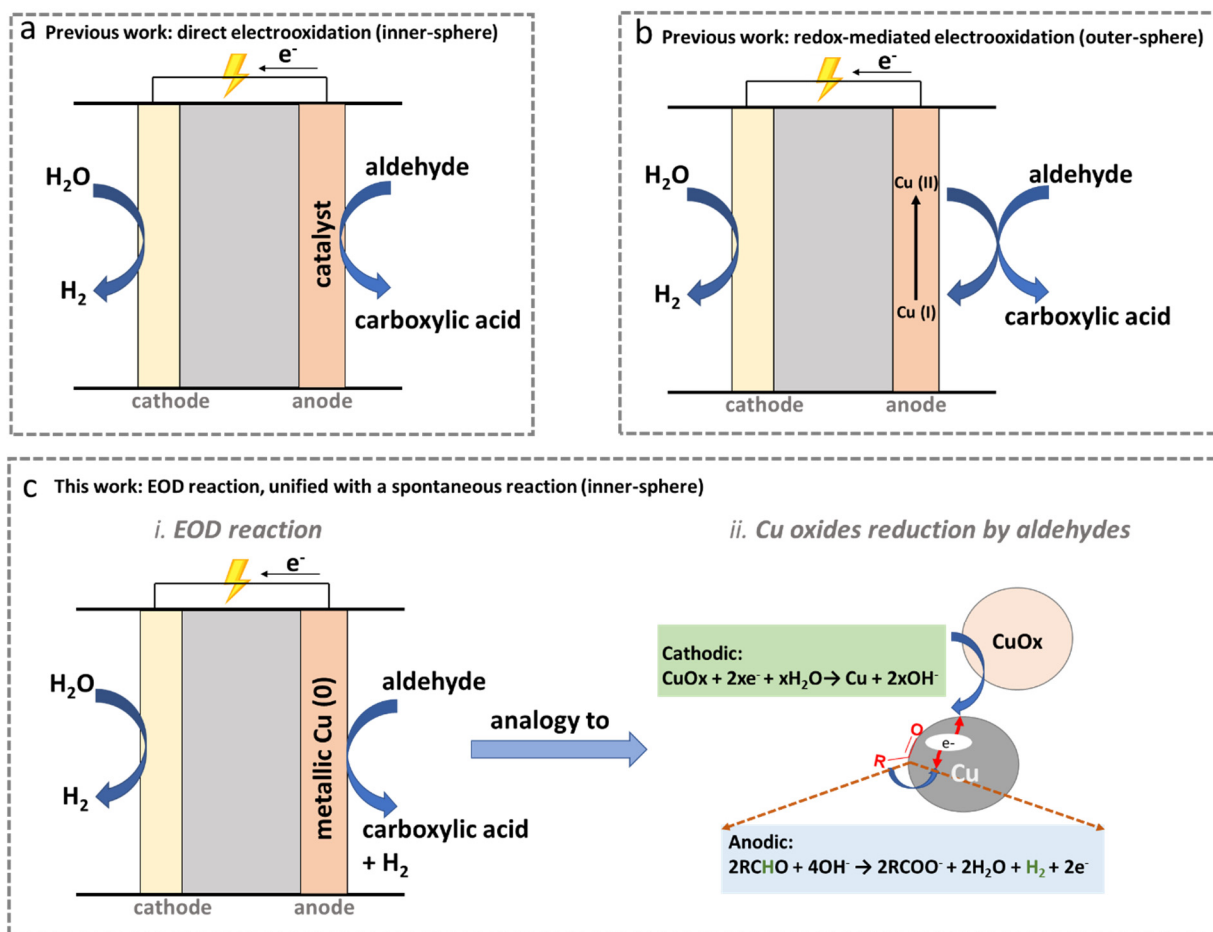


**Fig. S12 Comparison of various electrochemical and thermochemical systems of aldehydes oxidation.** Scheme of (a) a direct<sup>20, 21</sup> and (b) a Cu(I)/Cu(II) redox-mediated process<sup>22, 23</sup> for electrooxidation of aldehyde toward carboxylic acid without H<sub>2</sub> evolution. (c) Scheme of EOD reaction toward carboxylic acid and H<sub>2</sub> that was catalyzed by metallic Cu. It is unified with a spontaneous reaction: Cu oxides reduction by aldehydes along with H<sub>2</sub> evolution.

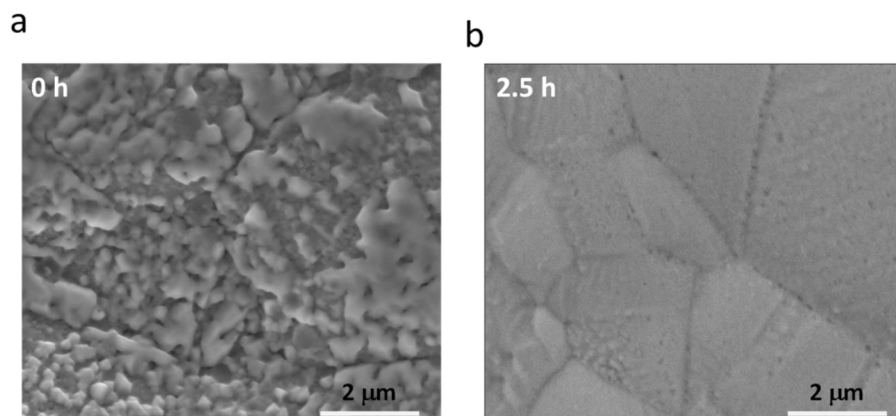


**Fig. S13 SEM of OD-Cu before and after electrolysis at 0.2 V<sub>RHE</sub>.**

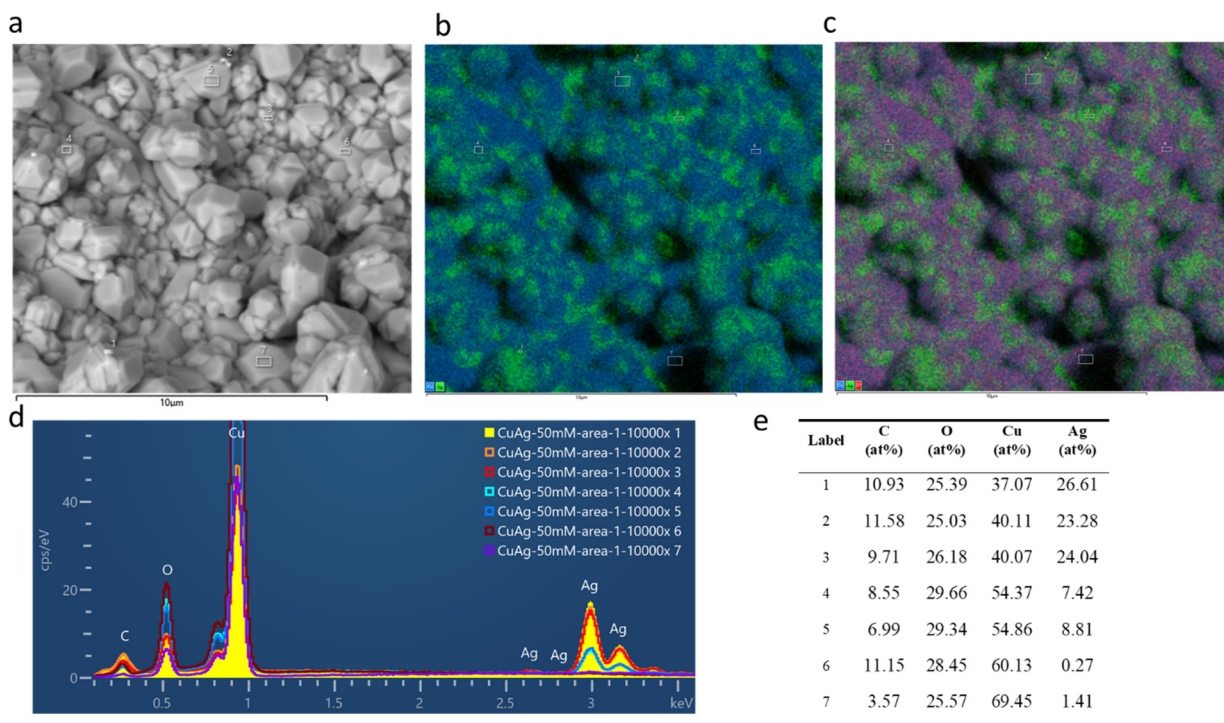


**Fig. S14 SEM-EDS analysis of as-synthesized CuAg<sub>glv</sub>/Cu electrode.** (a) SEM image and (b)-(e) EDS analysis of the as-synthesized CuAg<sub>glv</sub>/Cu. **Cu: blue; Ag: green; O: red.** It shows the coexistence of Cu oxide and metallic Ag on the porous surface of Cu foam. From SEM image, we did not observe significant amount of Ag nanoparticles on the Cu surface, but strong signal of Ag was detected from EDS, indicating Ag nanoparticles are mostly distributed underneath the Cu surface (within 1 μm depth). Atomic analysis showed that the Cu:O ratio is ~2:1 in most detected areas, indicating the formation of Cu<sub>2</sub>O on the surface.

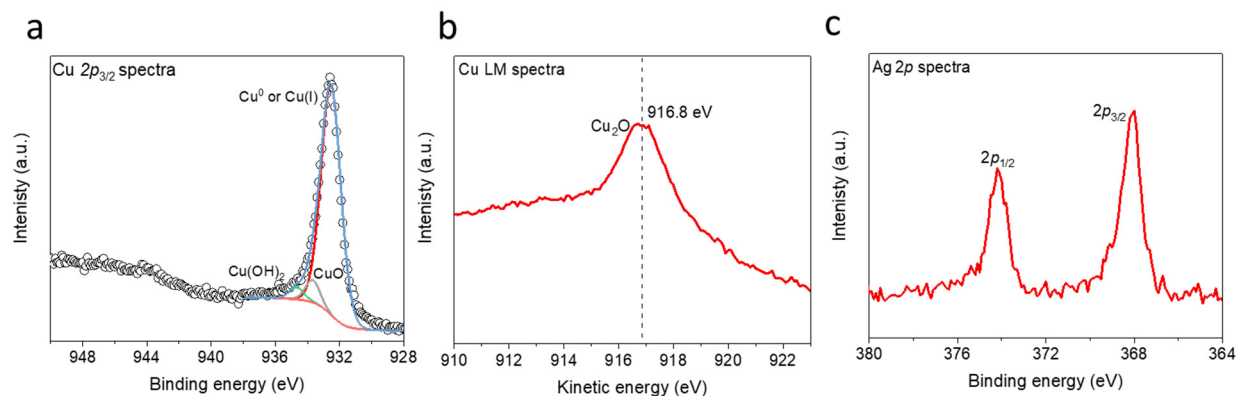


**Fig. S15 XPS of as-synthesized CuAg<sub>glv</sub>/Cu electrode.** (a) Cu 2p<sub>3/2</sub>, (b) Auger Cu LM, and (c) Ag 2p spectra on as-synthesized CuAg<sub>glv</sub>/Cu.

### XRD and XPS analysis of as-synthesized CuAg<sub>glv</sub>/Cu

The XRD patterns (**Fig. 3b**) of as-synthesized CuAg<sub>glv</sub>/Cu anode can be indexed to the characteristic diffraction peaks of Cu (PDF #00-004-0836), Cu<sub>2</sub>O (PDF #00-005-0667) and Ag (PDF #00-004-0783). Three phases on the as-synthesized CuAg/Cu foam were observed from XRD: copper, cuprite (Cu<sub>2</sub>O), and silver. Both metals are polycrystalline, and no evidence of Cu-Ag intermetallic was observed.

To further investigate the composition of Cu and Ag on the surface, XPS was performed (**Fig. S15**). The strong peak of Cu 2p<sub>3/2</sub> at ~932.6 eV corresponds to Cu(0) or Cu(I) state, which cannot be differentiated from the Cu 2p spectra.<sup>24</sup> According to Auger peak of Cu LM spectra at ~916.8 eV, the surface is indeed dominated by Cu(I) oxide. The fitted Cu 2p<sub>3/2</sub> peaks at ~933.8 eV and 934.7 eV are assigned to Cu(II) oxide and Cu(II) hydroxide, respectively. Ag is also present on the surface in its metallic state with a low atomic concentration (4.3 at%, **Table S7**). Because Cu<sub>2</sub>O is observed from XRD, EDS, and XPS, it exists on both the surface and bulk regions.

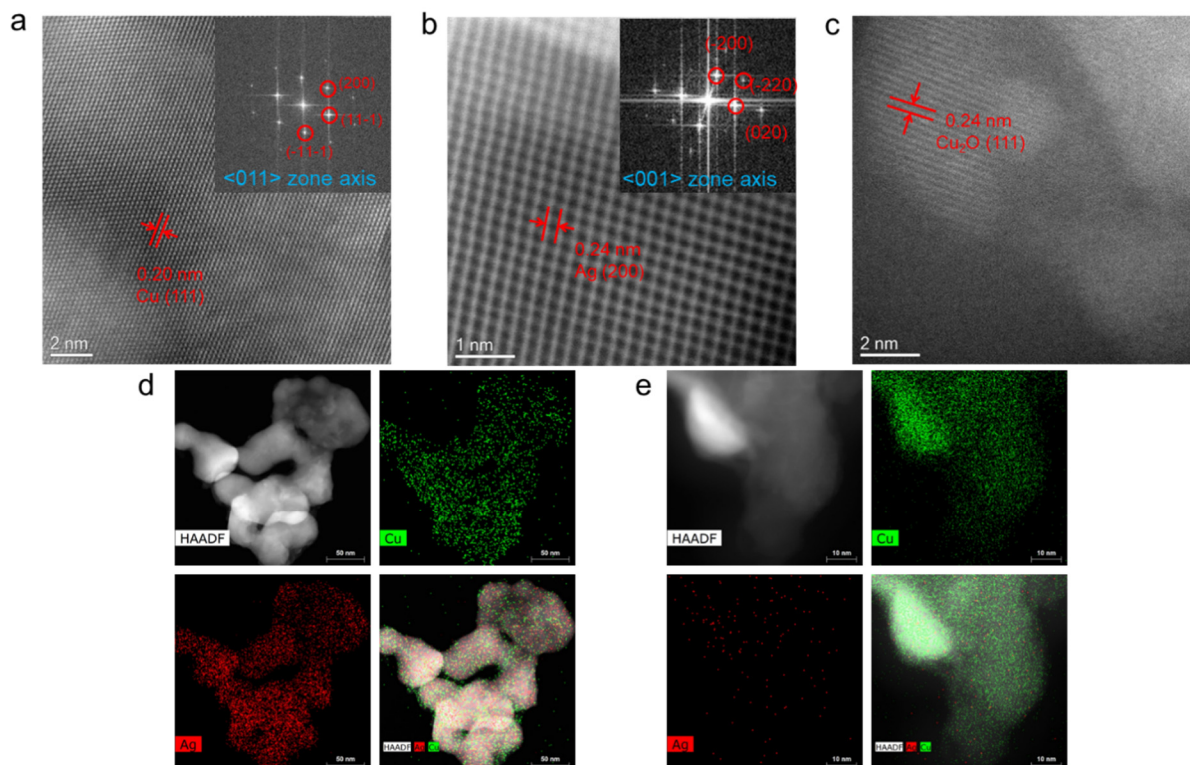


**Fig. S16 HRTM and HAADF-STEM-EDS mapping of CuAg<sub>glv</sub>/Cu electrode.** (a), (b), and (c) HRTEM images of Cu, Ag, and Cu<sub>2</sub>O region. Inset: Fast Fourier Transform (FFT) pattern. HRTEM images showed the lattice spacing of Cu and Cu<sub>2</sub>O, which agreed with the calculated lattice spacing from Fourier transform (FFT). (d) and (e) HAADF-EDX elemental mapping of two different regions. The HADDF-EDX pattern showed a uniformly distributed Ag (red color) on Cu substrate (green color).

Interestingly, we found that the tested Ag (200) lattice (0.24 nm) is larger than its theoretical value of 0.20 nm. This suggests some degree of Cu dissolution in the Ag phase. It has been revealed that Cu and Ag showed limited surface miscibility,<sup>25</sup> because they are completely immiscible in their entire composition at room temperature.<sup>26</sup> In fact, the addition of Ag adatoms onto Cu was found to spontaneously result in the formation of a random substitutional surface alloy at room temperature with a maximum Ag content of ~16 at.% in the top layer of atoms.<sup>25, 27</sup> Similar observation is also obtained from a previous work for ZnCu bimetal that were also prepared from the galvanic replacement method at room temperature.<sup>28</sup>

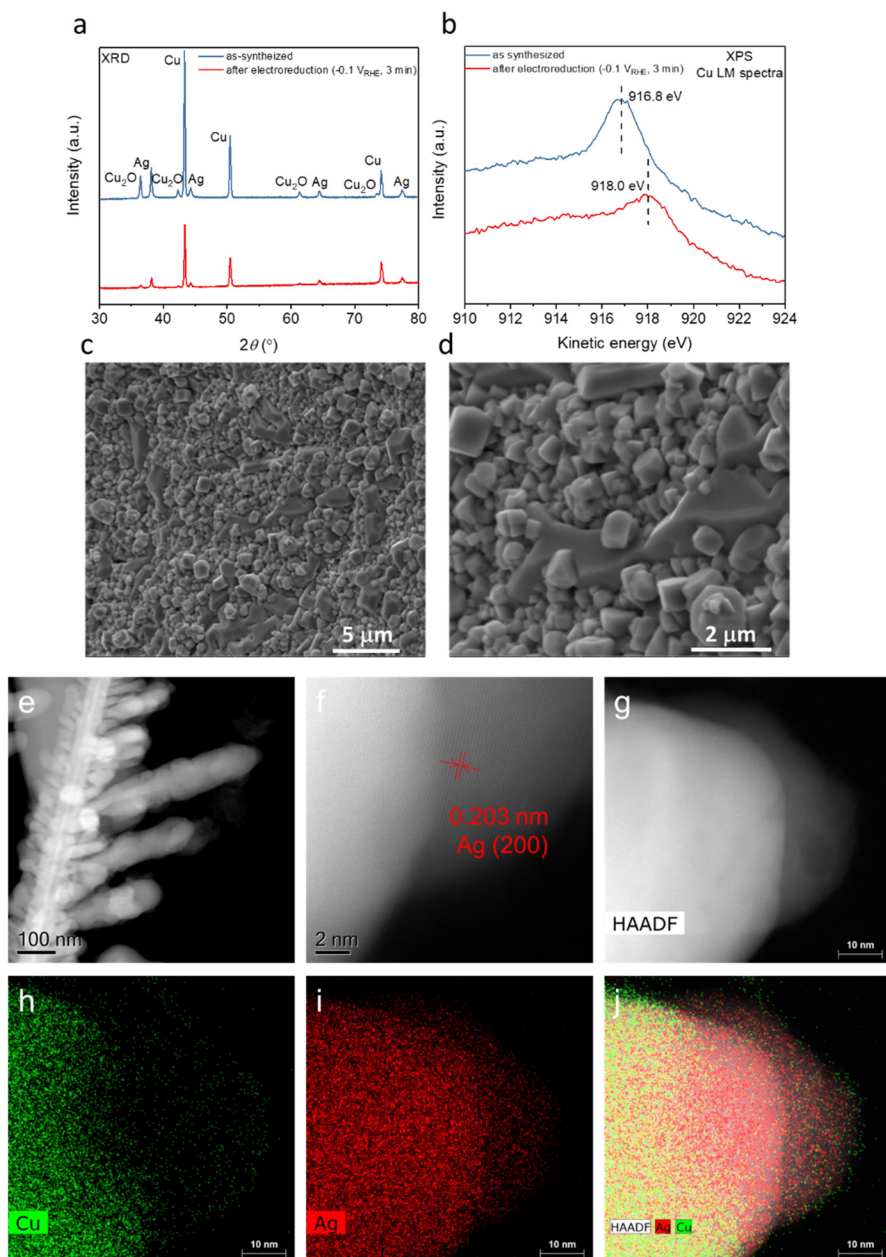


**Fig. S17** (a) EX-situ XRD pattern and (b) Auger peak of Cu LM spectra of CuAg<sub>glv</sub>/Cu before and after electroreduction at  $-0.1 V_{RHE}$  for 3 min. The reduction of CuAg<sub>glv</sub>/Cu was performed in the electrolyte with 200 mM furfural in 1 M KOH. (c)-(d) SEM images of the CuAg<sub>glv</sub>/Cu after electroreduction at  $-0.1 V_{RHE}$  for 3 min. (e)-(f) HRTEM images of Ag region. (g)-(j) HAADF-EDX elemental mapping of one region that showed a uniformly distributed Ag (red color) on Cu substrate (green color).

After reduction, the intensity of Cu<sub>2</sub>O peaks from XRD decreased significantly. Meanwhile, Cu LM spectra showed a kinetic energy shift from 916.8 eV to 918.0 eV, also suggesting the surface has been reduced to metallic Cu.<sup>24</sup> Both results indicated the *in-situ* transformation from a Cu<sub>2</sub>O-dominated surface to an oxide-derived CuAg<sub>glv</sub>/Cu surface. In addition, the porous electrode surface and uniform distribution of Ag on Cu was maintained.

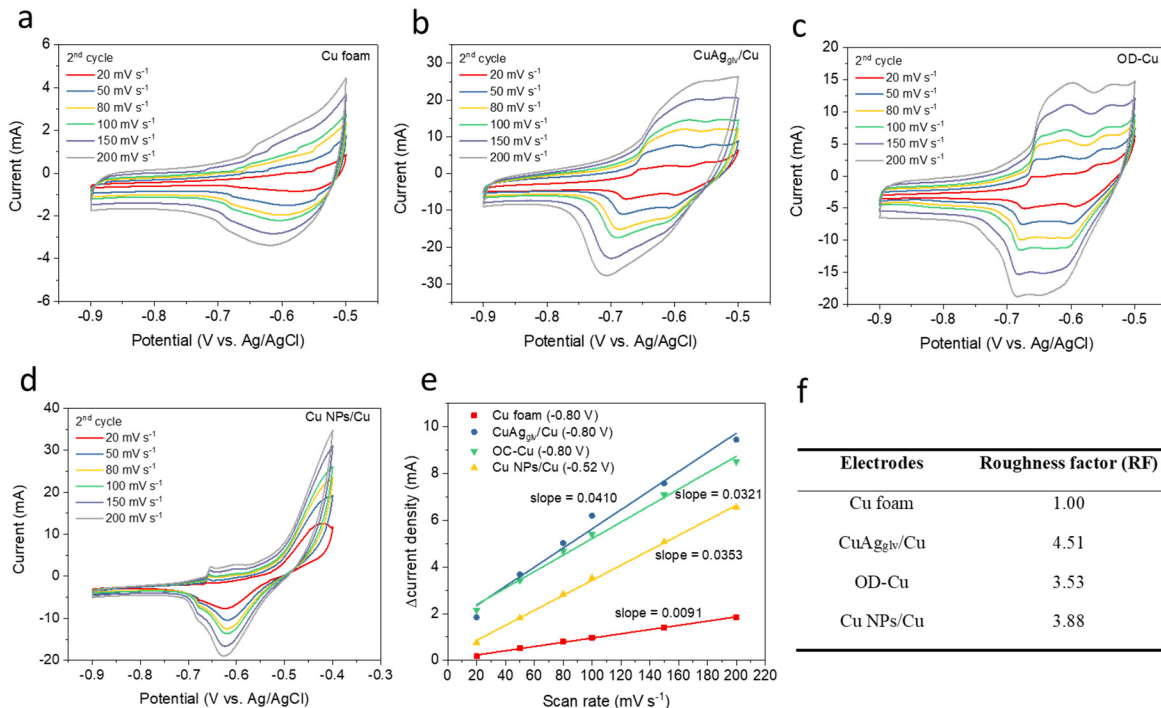


**Fig. S18 Roughness factors of Cu-based electrodes.** Cyclic voltammograms (CV, 2<sup>nd</sup> cycle) on Cu based electrodes: (a) Cu foam, (b) CuAg<sub>glv</sub>/Cu, (c) OD-Cu, and (d) Cu NPs/Cu. (e) The double-layer capacitance ( $C_{dl}$ ) was calculated on Cu-based electrodes at non-Faradaic regions. (f) Summary of the roughness factor normalized based on the Cu foam.

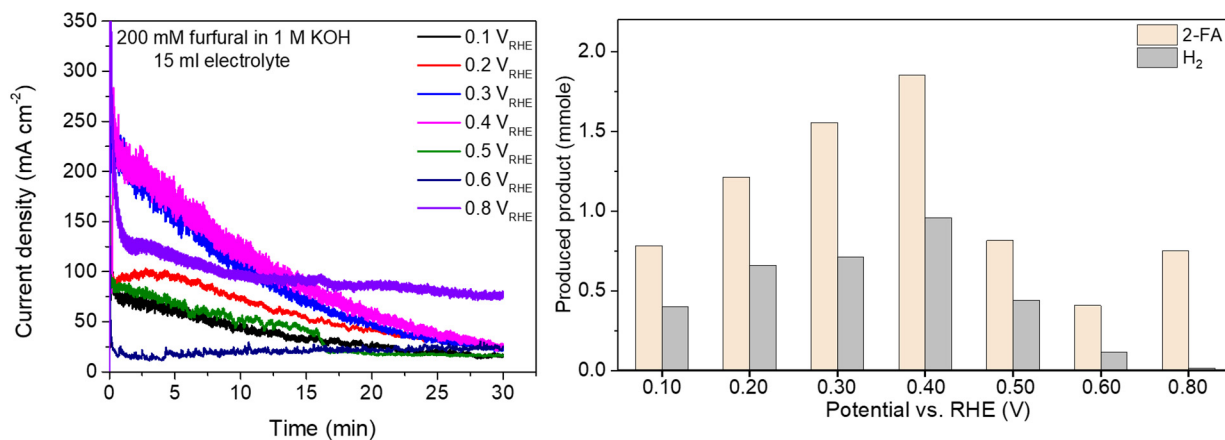


**Fig. S19** (a) Current density – time profiles and (b) products of EOD reaction on CuAg<sub>glv</sub>/Cu electrode at different potentials for half-hour electrolysis.

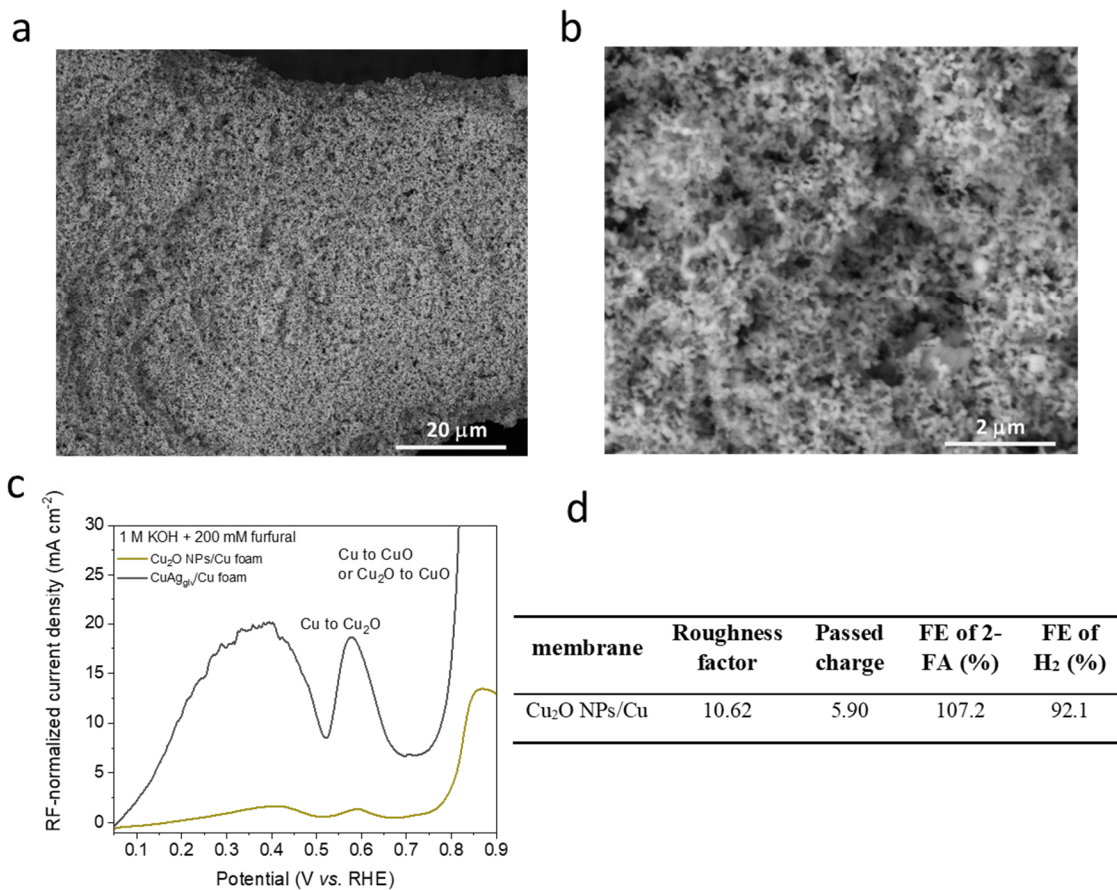


**Fig. S20 EOD reaction on Cu<sub>2</sub>O NPs/Cu electrode.** (a)-(b) SEM images. (c) LSV (2<sup>nd</sup> cycle) on Cu<sub>2</sub>O NPs/Cu and CuAgglv/Cu in 1 M KOH with 200 mM furfural. The current density is normalized based on the roughness factor (RF). (d) Summary of the results for half-hour electrolysis on Cu<sub>2</sub>O NPs/Cu.

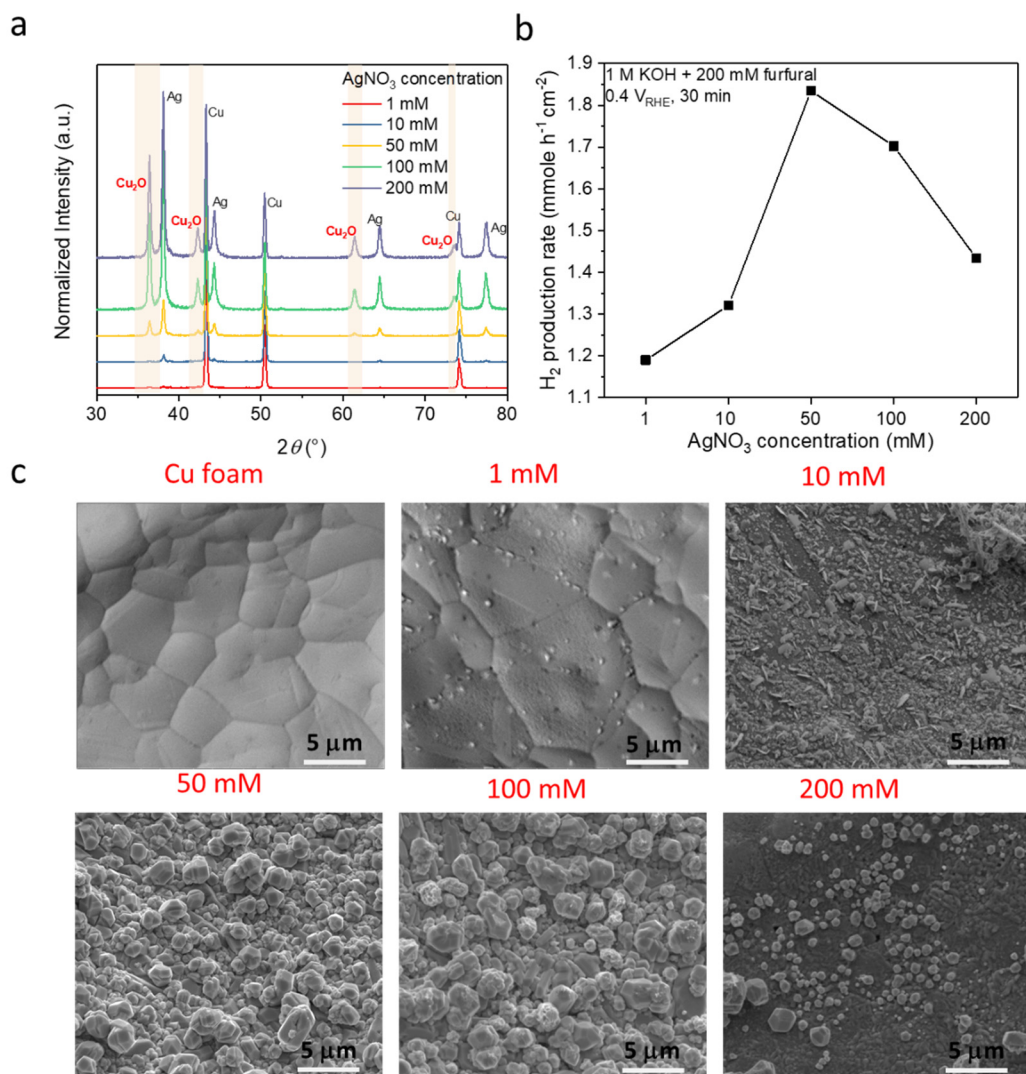


**Fig. S21 Characterizations and reaction activities of CuAg<sub>glv</sub>/Cu electrodes prepared with different precursor concentrations.** (a) XRD pattern. (b) H<sub>2</sub> production rate for half-hour electrolysis. (c) SEM images.

The XRD peaks for different samples were manually normalized to Cu (111) peak at 43.3°, then the relative abundance of all the other peaks can be compared directly, showing stronger intensities of Cu<sub>2</sub>O and Ag by increasing the concentration of AgNO<sub>3</sub>.

## Supplementary information note 2, analysis of surface reconstruction and protection effect of Ag

The trend of Cu:Ag value obtained from XPS is similar to those from EDS (Table S7). The as-prepared sample has a high Cu:Ag ratio, which decreased significantly after half-hour electrolysis and increased after 3.5-hour electrolysis. Interestingly, the percentage of Ag extracted from the surface-sensitive XPS analysis was generally higher than that from the EDS analysis, indicating some of the Ag beneath the surface Cu, because the "excitation depth" is much lower on XPS as compared to EDS: 5 nm vs.  $\sim 1 \mu\text{m}$ .

The cross-section SEM images (Fig. S24-25) were preceded by embedding the samples using a vacuum impregnation device. Then, epoxy was introduced to infiltrate the samples effectively and gently for subsequent polishing through 0.25- $\mu\text{m}$  diamond slurry. The images showed that most of Ag is filled within the interspace of the Cu foam. In the as-synthesized sample, Ag uniformly covers the outer surface of the Cu. From the Pourbaix diagrams (Fig. S28), Ag is more stable than Cu under our electrolysis condition of pH 14. Thus, the coverage of Ag layer can partly protect Cu and avoid its corrosion in the strong alkaline and anodic electrolytic conditions. However, for very long-term electrolysis, the Ag layer would become loose and gradually detach from the Cu surface, which is reflected in the performance decrease (21% after 7 cycles electrolysis) in the main text.

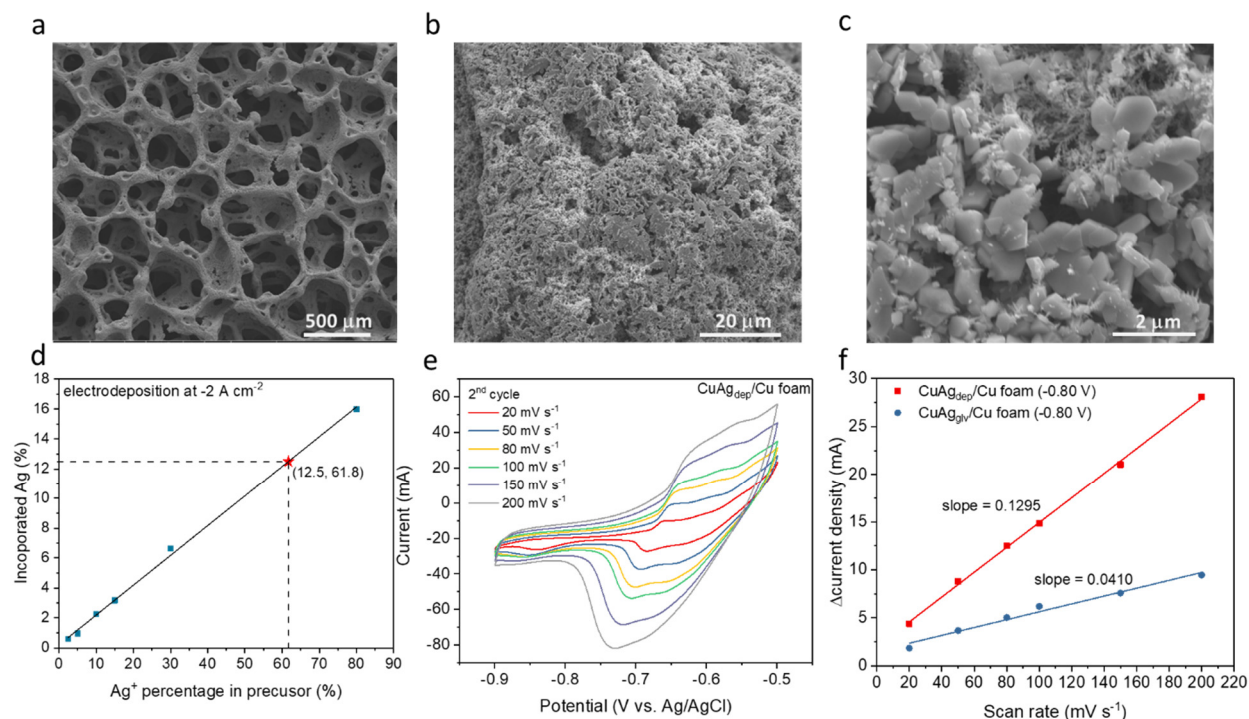


**Fig. S22 Characterization of CuAg<sub>dep</sub>/Cu.** (a)-(c) SEM images. (d) The relationship between the incorporated percentage of Ag probed by ICP-MS in the CuAg<sub>dep</sub>/Cu electrodes and the percentage of precursor [Ag<sup>+</sup>] in the electrolyte. The total precursor (AgNO<sub>3</sub> and CuSO<sub>4</sub>) concentration is kept at 50 mM. The co-electrodeposition is performed at 2 A cm<sup>-2</sup>.

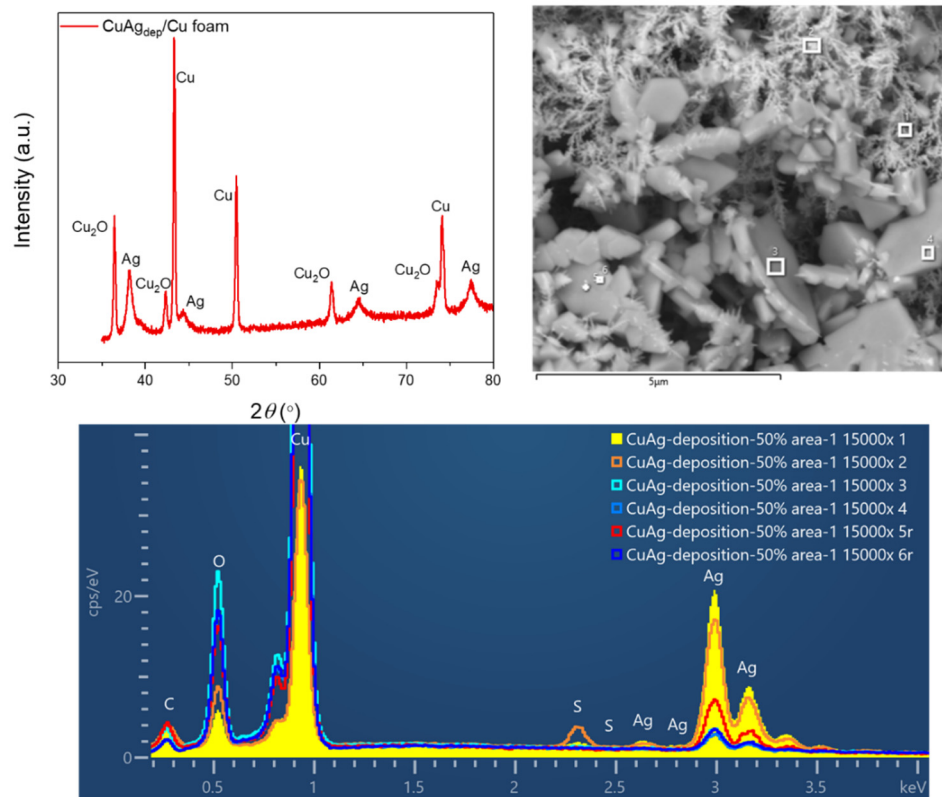


**Fig. S23** Characterization of CuAg<sub>dep</sub>/Cu. (a) XRD pattern and (b)-(c) SEM-EDS images.

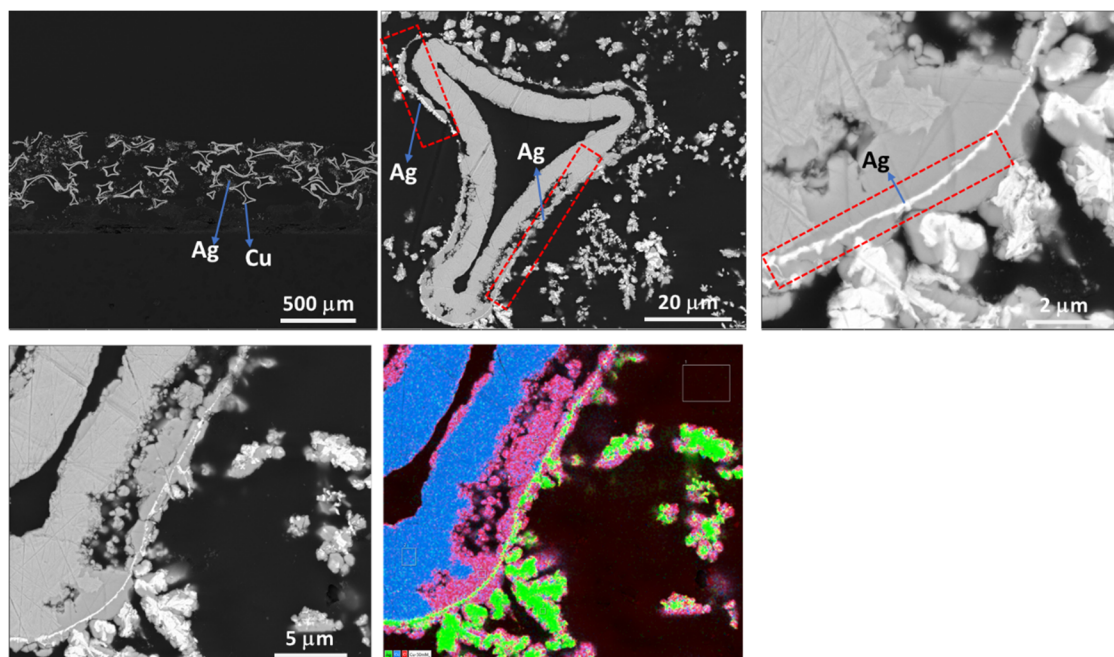


**Fig. S24** Cross-sectional SEM-EDS analysis of as-synthesized CuAg<sub>glv</sub>/Cu. Cu: blue; Ag: green; O: red.

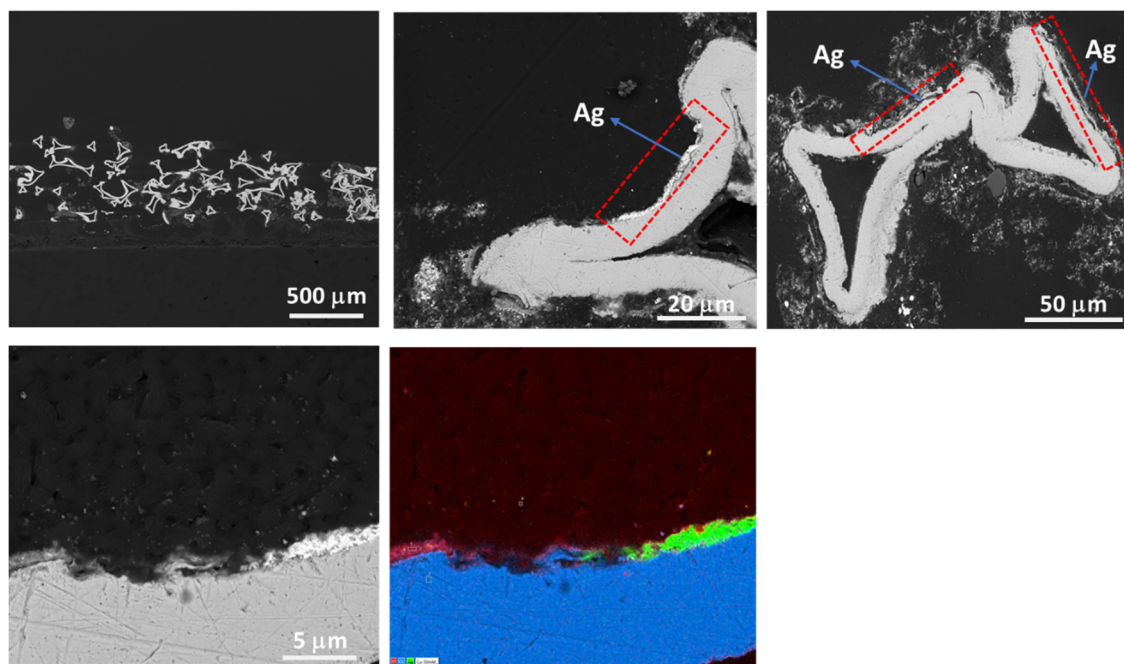


**Fig. S25** Cross-sectional SEM-EDS analysis of  $\text{CuAg}_{\text{glv}}/\text{Cu}$  after 3.5 hour-electrolysis at 0.2  $V_{\text{RHE}}$ . Cu: blue; Ag: green; O: red.

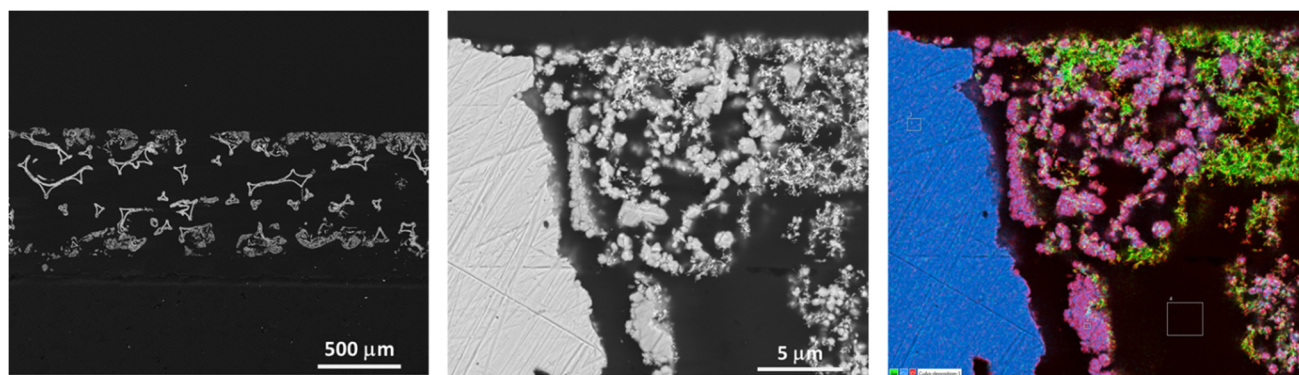


**Fig. S26** Cross-sectional SEM-EDS analysis of as-synthesized  $\text{CuAg}_{\text{dep}}/\text{Cu}$ . Cu: blue; Ag: green; O: red.

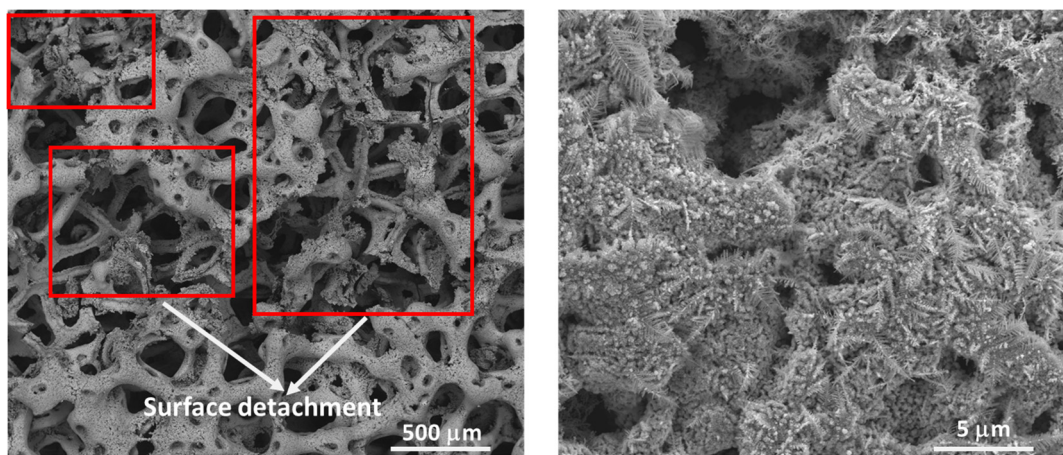


**Fig. S27** SEM images of  $\text{CuAg}_{\text{dep}}/\text{Cu}$  after 3.5-hour electrolysis at  $0.2 \text{ V}_{\text{RHE}}$ .

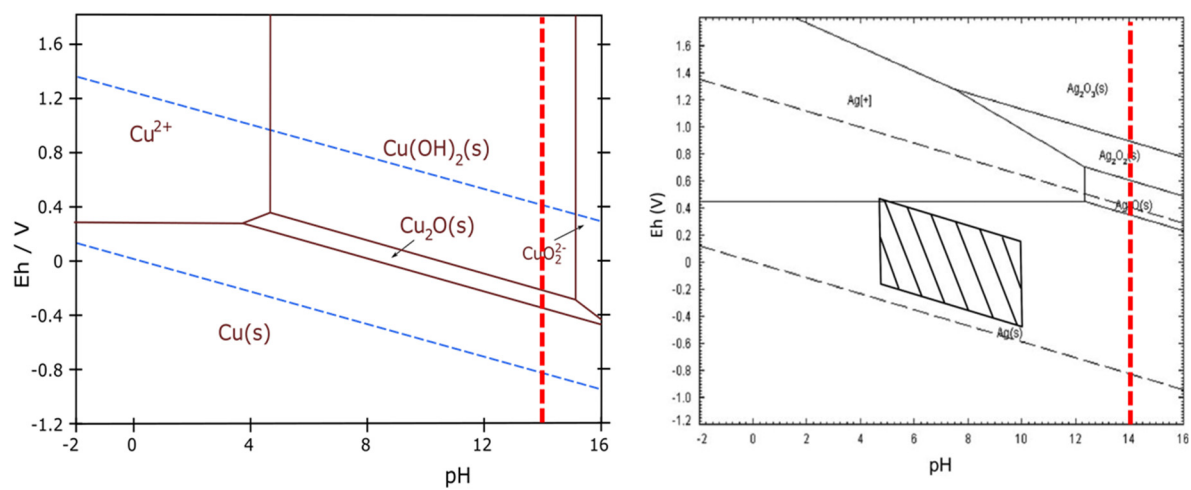


**Fig. S28** Pourbaix diagrams of Cu and Ag. These pictures are adapted from the literature.<sup>29-30</sup>

### Supplementary information note 3, characterization of CuAg<sub>glv</sub>/Cu at different stages of reaction

SEM and EDS analysis were performed at different reaction durations. SEM-EDS (**Fig. S29a**) on as-synthesized CuAg<sub>glv</sub>/Cu showed the homogeneous distribution of Ag on Cu foam, and an average Cu/O atomic ratio of 54:24, corresponding to Cu<sub>2</sub>O. After half-hour EOD reaction at 0.2 V<sub>RHE</sub> (**Fig. S29b**), small Ag clusters are dispersed on Cu surface with a significantly increase in Ag content. Ag-rich areas showed particle sizes of ~100 nm. From typical EDS mappings on Ag-rich regions, the green and light blue areas indicated thick Ag layers and Cu below the Ag layers, respectively. After prolonged electrolysis for 3.5 hours (**Fig. S29c**), the surface was predominated by CuO and showed nanorods morphology, indicating a dynamic transformation of surface Cu(I) to Cu (II).

XRD was applied to examine the phase purity of the catalysts and to track the evolution of the crystal structure after EOD reaction. XRD patterns showed the as-synthesized CuAg<sub>glv</sub>/Cu (**Fig. S30**) with the reflections assigned to Cu, Cu<sub>2</sub>O, and Ag. After half- and 3.5-hour EOD reactions at 0.2 V<sub>RHE</sub>, Cu<sub>2</sub>O was fully reduced to metallic Cu.

XPS measurements were conducted to gain deeper insights into the surface composition and chemical state of the CuAg<sub>glv</sub>/Cu before and after EOD reactions. The Ag<sub>3d</sub> core-level regions of CuAg<sub>glv</sub>/Cu revealed that Ag is in the metallic state before and after EOD reactions, consistent with XRD results. In the deconvoluted Cu 2p<sub>3/2</sub> spectra (**Fig. S31**), a main peak is observed at the binding energy of 932.6 eV together with two peaks at 933.6 eV and 934.8 eV, representing the signals of Cu(0)/Cu<sub>2</sub>O, CuO, and Cu(OH)<sub>2</sub>, respectively.<sup>24</sup> The metallic Cu and Cu<sub>2</sub>O signal cannot be differentiated from Cu 2p spectra. The surface composition ratios of Cu(0 or I)/Cu (II) were determined by integrating the fitted peak areas between Cu (0 or I) and Cu (II) [CuO and Cu (OH)<sub>2</sub>]. Cu(II) percentage in the as-synthesized sample is minor (<15%), which has increased to ~45% when the electrolysis duration exceeded a half hour. The Cu(II) satellite peak at ~944 eV also suggested the transformation of the Cu chemical state to Cu(II) after EOD reactions. In particular, the surface Cu(OH)<sub>2</sub> species has increased from 23.6% after 0.5 h to 41.1% after 3.5 h, which could be attributed to the slight decrease in EOD activity as observed from the main text. It is worth noting that the surface Cu(OH)<sub>2</sub> is commonly observed from XPS, especially when the electrolysis is performed in aqueous media.<sup>31, 32</sup> Additionally, Auger Cu LM spectra (**Fig. S32**) were also carried out to distinguish Cu(0), Cu(I), and Cu(II) species at near-surface regions. In the as-prepared sample, the peak at ~916.8 eV suggested the domination of Cu<sub>2</sub>O on its surface, agreeing with the EDS and XRD results. After EOD reactions of 0.5 and 3.5 hours, the gradually broadening of full width at half maximum (FWHM) and the shift of kinetic energy to lower values suggested the transformation of Cu<sub>2</sub>O to Cu(OH)<sub>2</sub>,<sup>24, 33</sup> consisted with Cu 2p spectra.

Unlike the XPS results, peaks for Cu(OH)<sub>2</sub> and CuO are not observed in XRD, which could be due to the amorphous nature of the phases and/or small domain sizes.<sup>34, 35</sup>

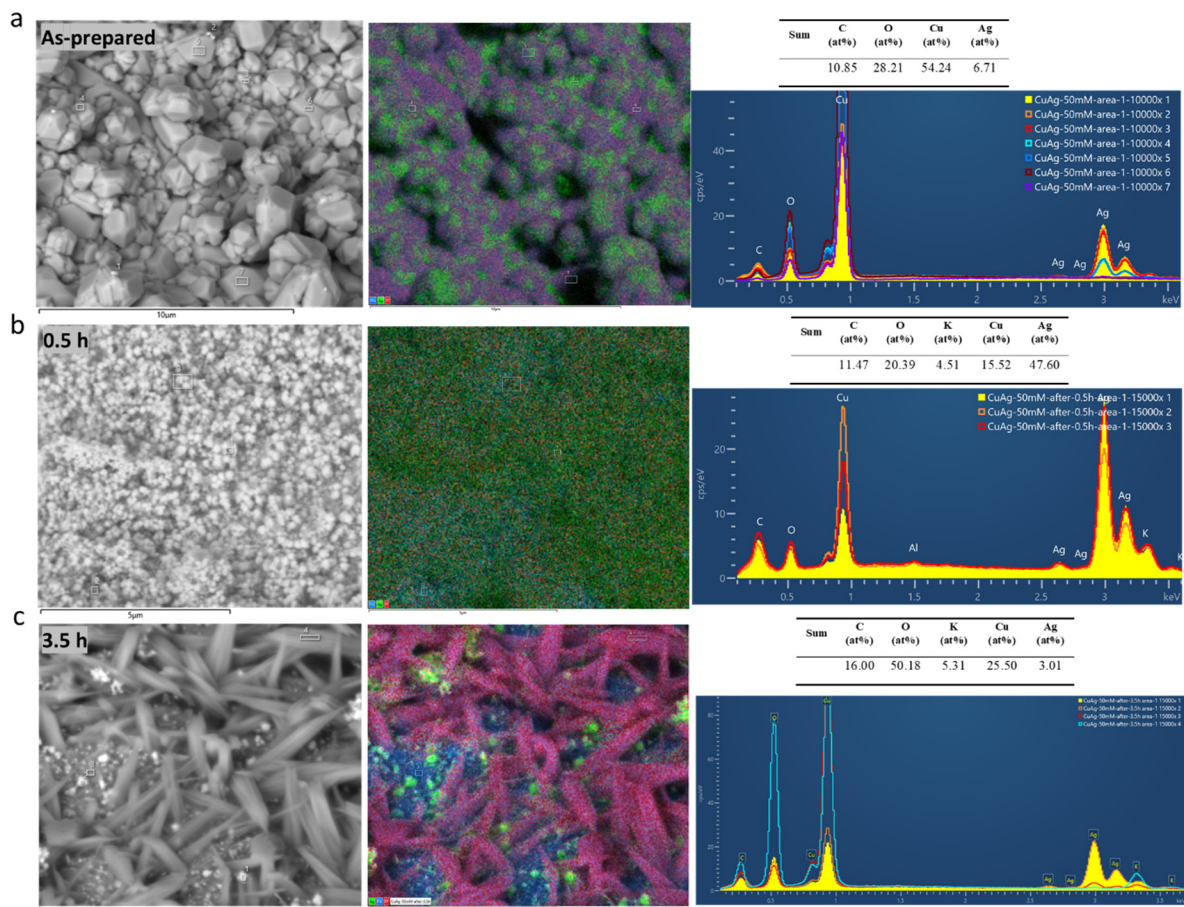


**Fig. S29** SEM-EDS analysis of CuAg<sub>glv</sub>/Cu before and after electrolysis at 0.2 V<sub>RHE</sub>. **Cu: blue; Ag: green; O: red.**

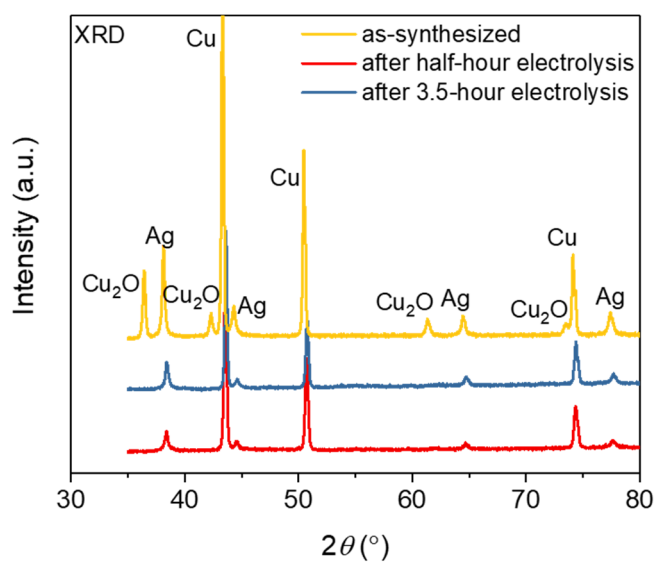


**Fig. S30** XRD patterns of CuAg<sub>glv</sub>/Cu before and after electrolysis at 0.2 V<sub>RHE</sub>.

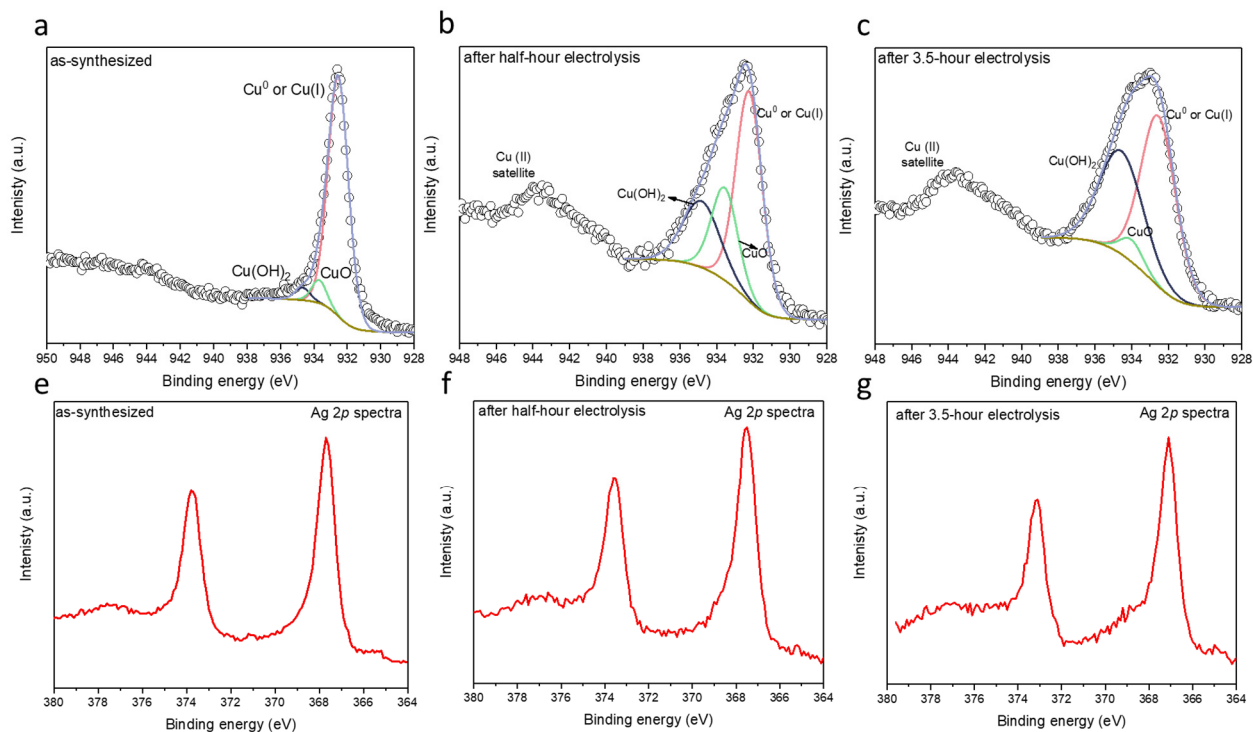


**Fig. S31** XPS analysis of CuAg<sub>glv</sub>/Cu at different reaction durations. The shoulder peak appeared at ~944 eV, suggesting the characteristic “shake up” satellite structure, which is typical for the Cu<sup>2+</sup> state.

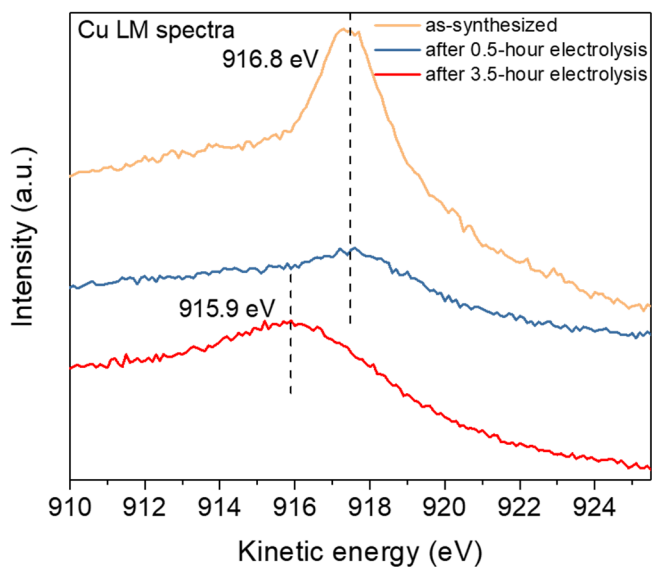


**Fig. S32** Auger electron spectra of Cu LM at different reaction durations for CuAg<sub>glv</sub>/Cu.

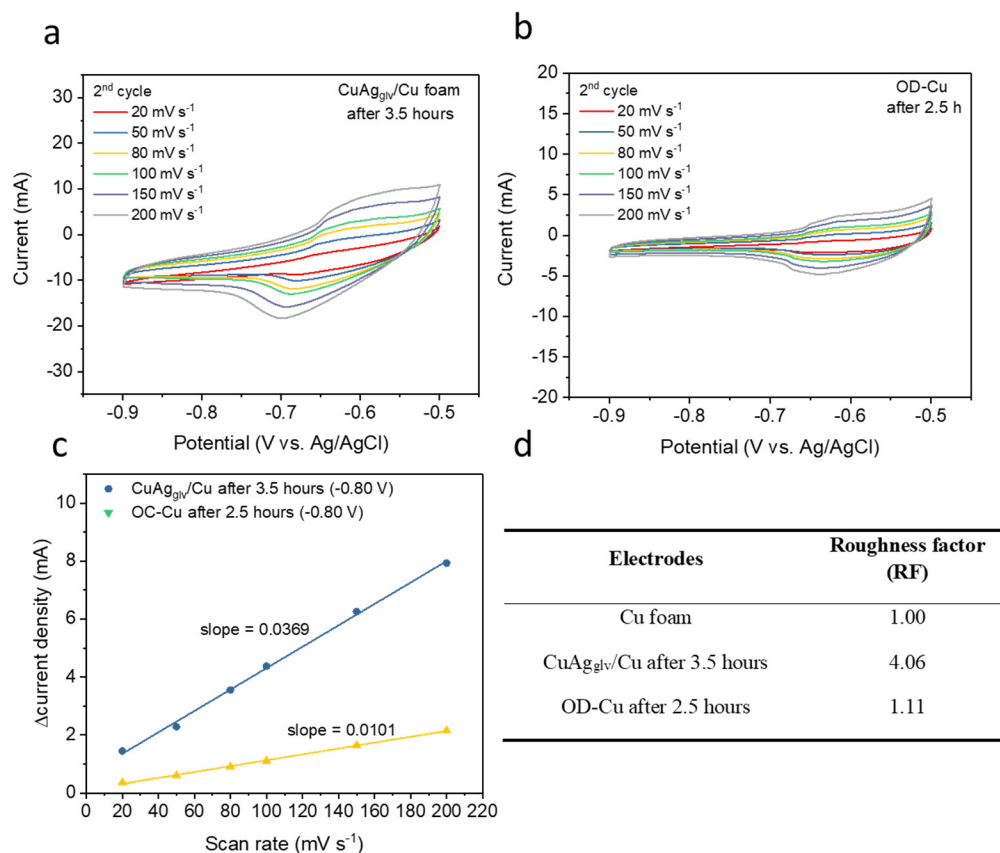


**Fig. S33** Roughness factor of CuAg<sub>glv</sub>/Cu and OD-Cu after electrolysis.

**Table S7.** Summary of Cu and Ag compositions at different reaction durations.

Time (h)	EDS		XPS	
	Cu (at%)	Ag (at%)	Cu (at%)	Ag (at%)
As synthesized	88.99	11.01	95.69	4.31
0.5	24.59	75.41	66.12	33.88
3.5	89.44	10.56	92.58	7.42

**Table S8.** ICP results of CuAg<sub>glv</sub>/Cu pre- and post-reaction.

	Percentage of Ag (%)	Dissolved Cu in electrolyte (ppm)	Dissolved Ag in electrolyte (ppm)
As synthesized	12.5	N/A*	N/A*
After 3.5-hour EOD reaction	11.8	1.78	0.57

\*: below ICP detection limit.

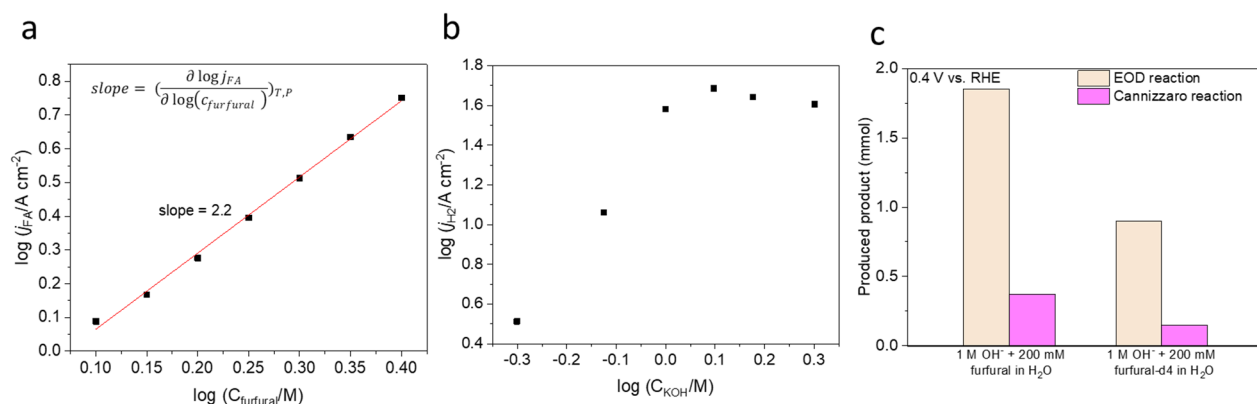


**Fig. S34 Electrokinetic studies for EOD reaction on CuAg<sub>glv</sub>/Cu.** (a) Reaction order fitting for Cannizzaro reaction (furfural-to-2-FA). (b) Dependence of partial current density of H<sub>2</sub> on base concentration. (c) Produced 2-FA for half-hour electrolysis at 0.4 V<sub>RHE</sub>.

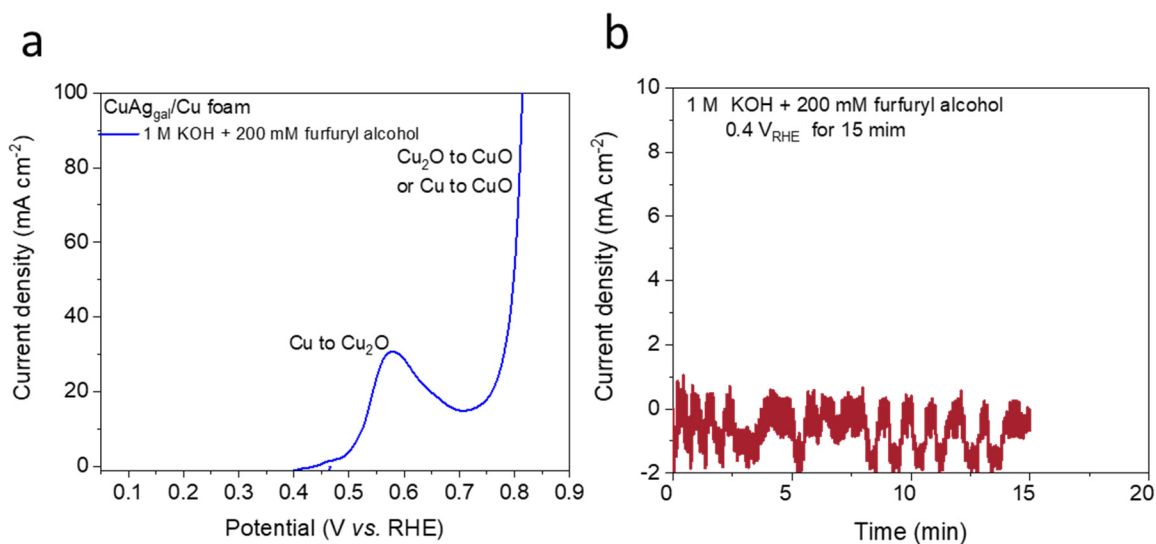


**Fig. S35 Control experiment of electrolysis with furfuryl alcohol on CuAg<sub>glv</sub>/Cu electrode.** (a) LSV and (b) CA curves on CuAg<sub>glv</sub>/Cu electrode. The current density at 0.4 V<sub>RHE</sub> is due to the background double layer charging-discharging.

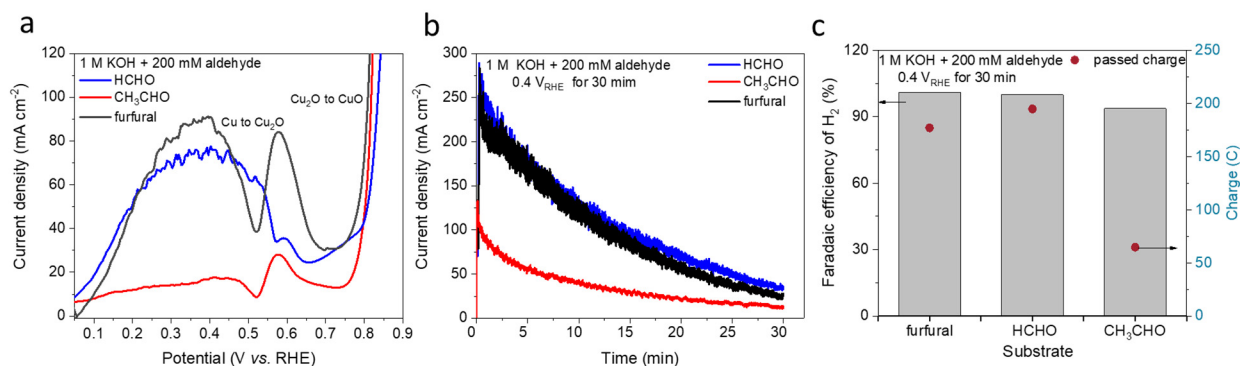


**Fig. S36 Extending EOD reactions to various feedstocks with or without  $\alpha$ -H.** (a) LSV (2<sup>nd</sup> cycle) in 1 M KOH with 200 mM of various aldehydes. (b) Current density-time profiles and (c) faradaic efficiency (left y-axis) and passed charge (right y-axis) of H<sub>2</sub> at 0.4 V<sub>RHE</sub> for half-hour electrolysis. The decrease in current density is due to the consumption of furfural.

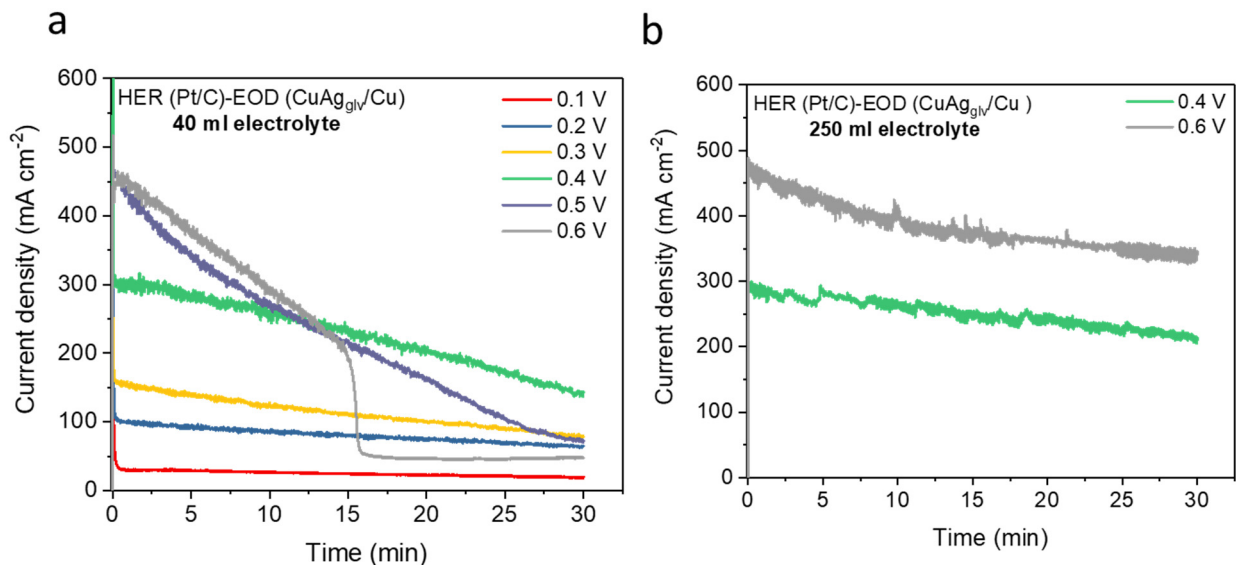


**Fig. S37 Current density-time profiles in the MEA-based flow cell.** The half-hour electrolysis was performed at different cell voltages with (a) 40 ml and (b) 250 ml electrolyte. The anolyte and catholyte were prepared in 1 M KOH solution with and without 250 mM furfural, respectively. The gradual decrease in current density is due to the consumption of reactant. In particular, at 0.6 V with 40 ml electrolyte, we observed a sharp decrease in current density at around 15 min. In the MEA-based flow electrolyzer, the voltage drops are attributed to the anodic EOD reaction, cathodic HER (minor but non-negligible), and membrane and solutions resistances. During electrolysis at 0.6 V, because of the consumption of furfural reactant, the voltage drops for HER and resistances are gradually lower and for anodic EOD reaction are higher. When the anodic potential higher than Cu oxidation, the surface would be oxidized to Cu(I), which has been confirmed not reactive for EOD reaction, resulting in a suddenly decrease in the current density. In contrast, when the solution volume was increased to 250 ml, the current density at both 0.4 and 0.6 V<sub>RHE</sub> became relatively stable during half-hour electrolysis.

**Table S9.** Comparison of the various types of paired systems for electrochemical H<sub>2</sub> production.

Paired types	Anodic reactant	Anode	Anode product	Cathode (for HER)	$j$ (mA cm <sup>-2</sup> ) <sup>b</sup>	Cell voltage	Ref.	
HER-ECO	HMF	Co-P/CF		Co-P/CF	20	1.39	36	
		Ni <sub>2</sub> P NPA/NF	2,5-furandicarboxylic acid	Ni <sub>2</sub> P NPA/NF	10	1.44	37	
		Ni <sub>3</sub> S <sub>2</sub> /NF		Ni <sub>3</sub> S <sub>2</sub> /NF	10	1.46	38	
		MoO <sub>2</sub> -FeP@C		MoO <sub>2</sub> -FeP@C	10	1.49	39	
	urea	Ni <sub>2</sub> Fe(CN) <sub>6</sub>		RuO <sub>2</sub>	100	1.35	40	
		Ni-WOx	N <sub>2</sub> and CO <sub>2</sub>	Ni-WOx	100	1.42	41	
		NiSe <sub>2</sub> -NiO		NiSe <sub>2</sub> -NiO	41	1.5	42	
		NF/NiMoO		NF/NiMoO	10	1.38	43	
	F-modified FeOOH			Pt/C	10	1.43	44	
	ethanol	SA In-Pt NWs/C		SA In-Pt NWs/C	10	0.62	45	
		glycerol	NC/Ni-Mo-N/NF	formate	NC/Ni-Mo-N/NF	10	1.38	46
	Ni-Mo-N/CFC		formate	Ni-Mo-N/CFC	10	1.36	47	
	glucose	NiFeOx-NF		NiFeOx-NF	100	1.39	48	
		Cu(I)/Cu(II) Redox	glucaric acid	Pt/C	100	0.92	49	
	raw biomass (chitin)	hp-Ni	acetic acid	hp-Ni	100	1.83	50	
	NO	carbon cloth	NO <sub>3</sub> <sup>-</sup>	N/A	10	1.39	51	
	ascorbic acid	Cu(I)/Cu(II) Redox	dehydroascorbic acid	CoP	100	0.94	52	
	HER-OER	H <sub>2</sub> O	Co-NC-T/CF		CoO-NC-T/CF	100	1.86	53
			NiFe-LDH	O <sub>2</sub>	Pt/C	280	1.7	54
IrO <sub>2</sub>			Pt black		399	1.8	55	
FeP/Ni <sub>2</sub> P			FeP/Ni <sub>2</sub> P		500	1.72	56	
Cu foam	Pt/C	100	0.31		57			
HER-EOD	furfural		Furoic acid and H <sub>2</sub>		248	0.4	This work	
		CuAg <sub>glv</sub> /Cu		Pt/C	390	0.6	This work	

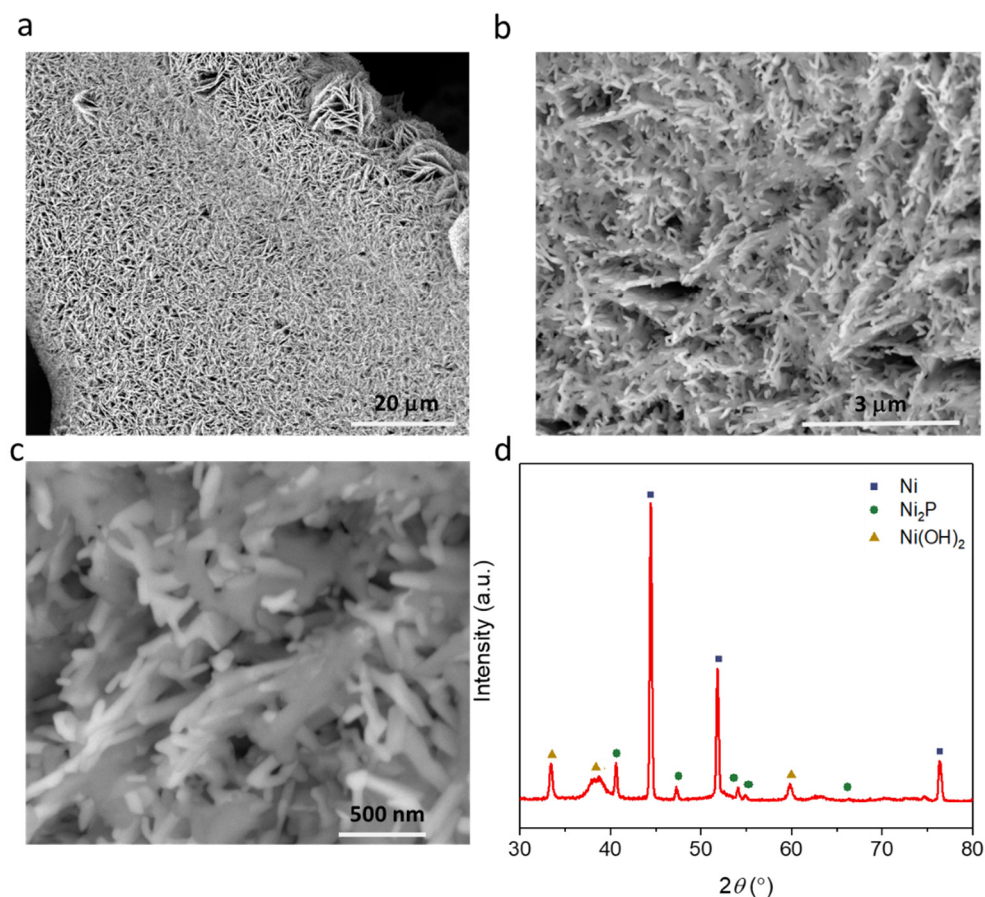


**Fig. S38 (a)-(c) SEM and (d) XRD patterns of Ni<sub>2</sub>P catalyst.** XRD pattern can be indexed to the characteristic diffraction peaks of Ni (PDF#04-0850), Ni<sub>2</sub>P (PDF#03-0953), and Ni(OH)<sub>2</sub> (PDF#38-0715).

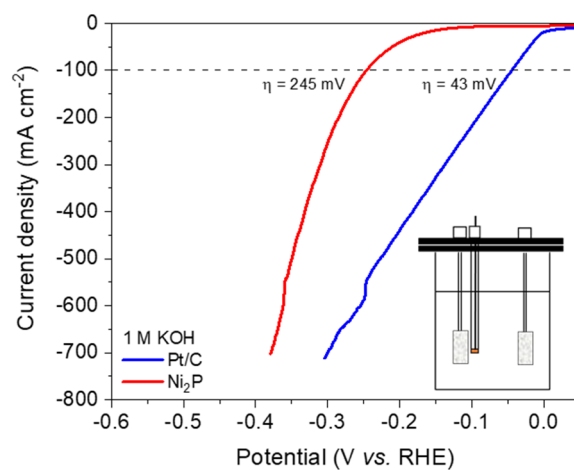


**Fig. S39 HER on Ni<sub>2</sub>P and Pt/C in a one-compartment cell with a three-electrode configuration.** The geometric area of electrode is 1 cm<sup>2</sup>, and the electrolyte is 1 M KOH.

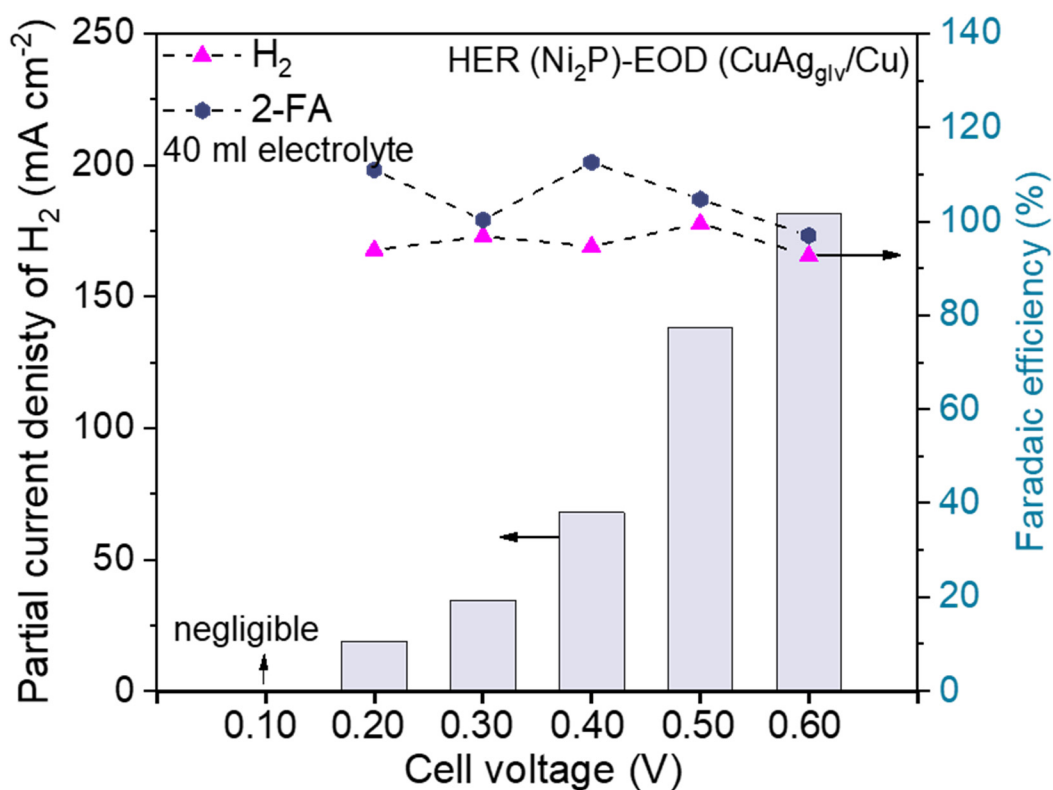


**Fig. S40** Bipolar H<sub>2</sub> production in the MEA-based flow cell (40 ml electrolyte) with CuAg<sub>glv</sub>/Cu anode and Ni<sub>2</sub>P cathode for half-hour electrolysis. The anolyte and catholyte were prepared in 1 M KOH solution with and without 250 mM furfural, respectively.

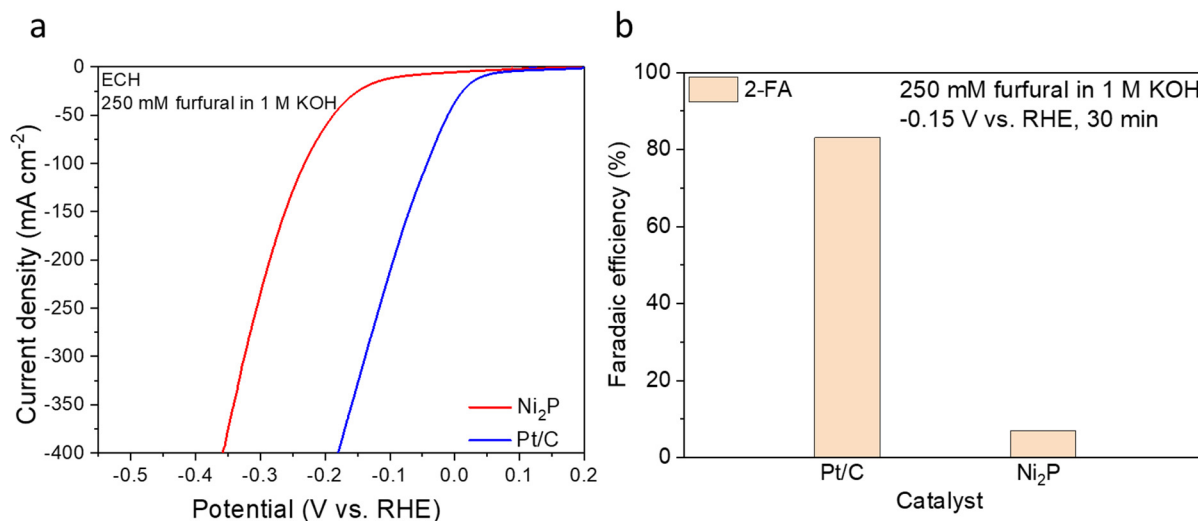


**Fig. S41** ECH of furfural on Ni<sub>2</sub>P and Pt/C in H-type cell. (a) Linear sweep voltammograms. (b) Faradaic efficiency for half-hour electrolysis in 1 M KOH with 250 mM furfural.

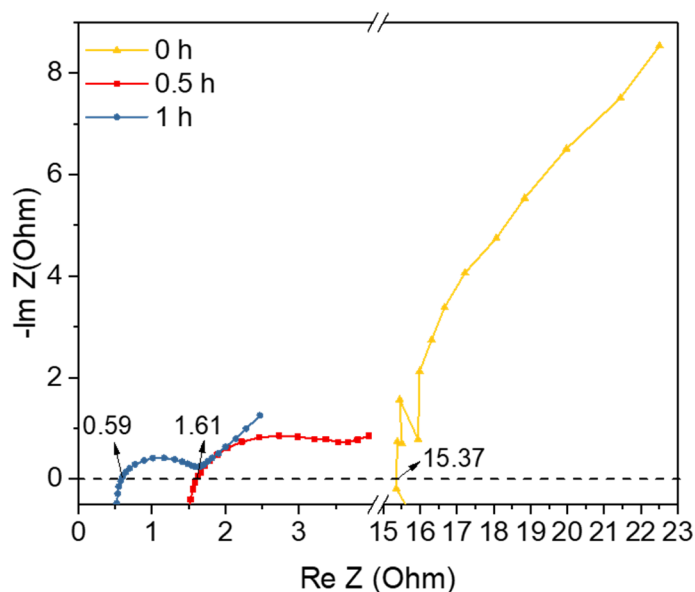


**Fig. S42 Electrochemical impedance spectroscopy of the MEA-based flow cell with dialysis membrane after different durations of pretreatment.** The membrane was treated by storing in 1 M KOH solution for different durations.

**Table S10.** Crossover of products after half-hour electrolysis at 0.4  $V_{RHE}$  in the flow cells with AEM or dialysis membrane.<sup>a</sup>

membrane	furfuryl alcohol (mM)	2-FA (mM)	furfural (mM)
AEM	3.67	7.15	N/A
Dialysis	4.19	2.02	0.34

a. The anolyte and catholyte were prepared in 1 M KOH with and without 250 mM furfural (40 ml electrolyte), respectively. The crossover was detected by quantification of the products in the catholyte after half-hour electrolysis.

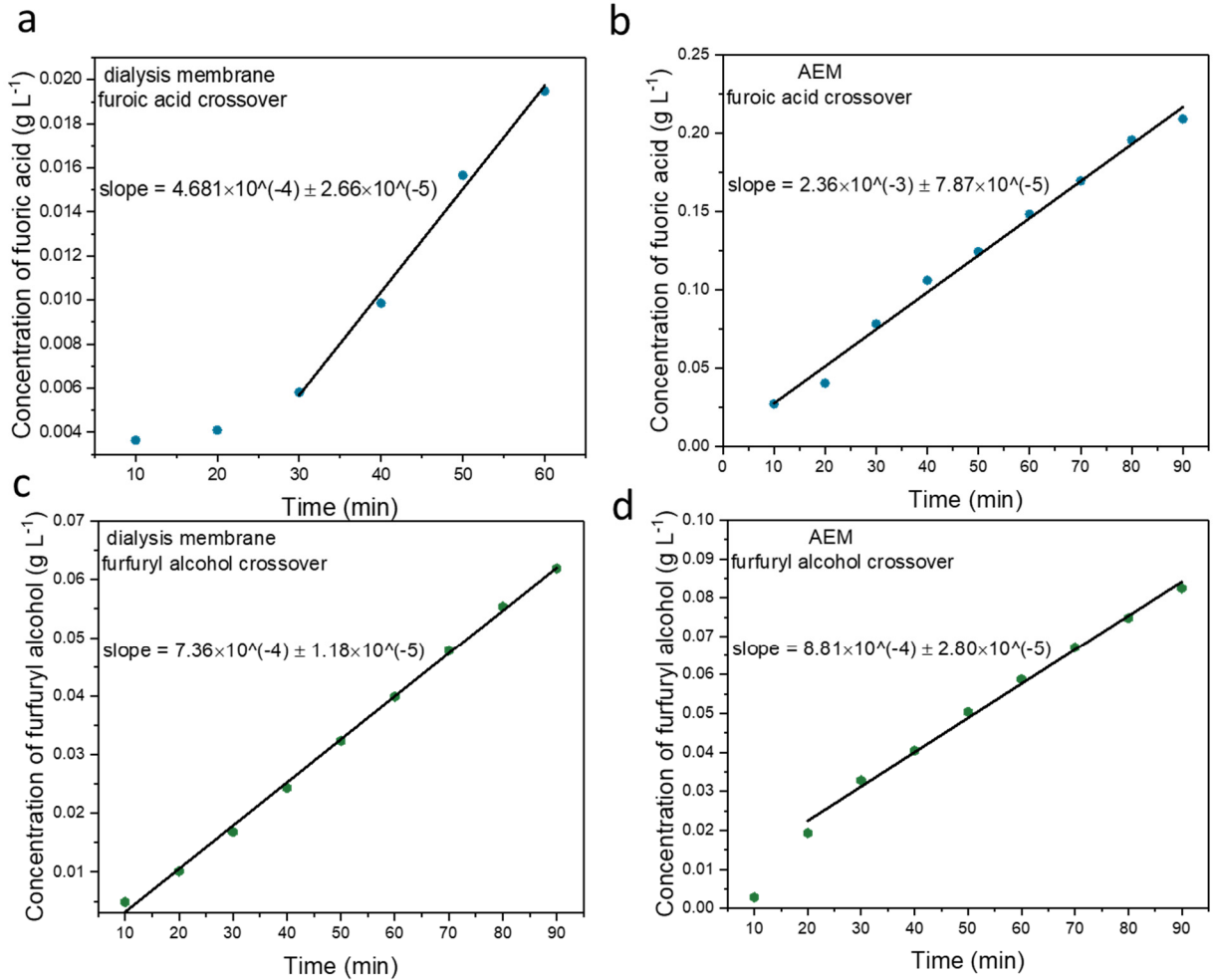


**Fig. S43 Crossover studies on dialysis membrane and AEM.** Time-dependent (a)-(b) 2-FA or (c)-(d) furfuryl alcohol concentration in the catholyte that was separated by a cellulose-based dialysis membrane or AEM. The catholyte was 1 M KOH, and anolyte was 1 M KOH with (a)-(b) 250 mM 2-FA or (c)-(d) furfuryl alcohol. The volume of catholyte and anolyte is 40 ml. All crossover experiments were performed in a similar MEA-based flow cell set-up with the Pt/C cathode and  $\text{CuAg}_{\text{glv}}/\text{Cu}$  anode under OCV. The permeability (details in the Experimental Methods) was determined by the equation as follow:

$$P_s = \frac{V_C}{c_A A} \frac{dc_C}{dt} = \frac{D_s}{L}$$

We have obtained the maximum permeability from the linear part of the diffusion graph. The permeability of 2-FA of dialysis membrane and AEM is  $P_{2\text{-FA, max}} = 5.56 \times 10^{-6} \text{ cm s}^{-1}$  and  $P_{2\text{-FA, max}} = 2.80 \times 10^{-5} \text{ cm s}^{-1}$ , respectively. Their diffusion coefficients are  $D_{s,2\text{-FA}} = 3.89 \times 10^{-8} \text{ cm}^2 \text{ s}^{-1}$  and  $D_{s,2\text{-FA}} = 1.96 \times 10^{-7} \text{ cm}^2 \text{ s}^{-1}$ .

Similarly, these values for furfuryl alcohol are:  $P_{2\text{-FA, max}} = 8.74 \times 10^{-6} \text{ cm s}^{-1}$  and  $P_{2\text{-FA, max}} = 1.05 \times 10^{-5} \text{ cm s}^{-1}$ .

$D_{s, \text{alcohol}} = 6.12 \times 10^{-8} \text{ cm}^2 \text{ s}^{-1}$  and  $D_{s, \text{alcohol}} = 7.33 \times 10^{-8} \text{ cm}^2 \text{ s}^{-1}$ .

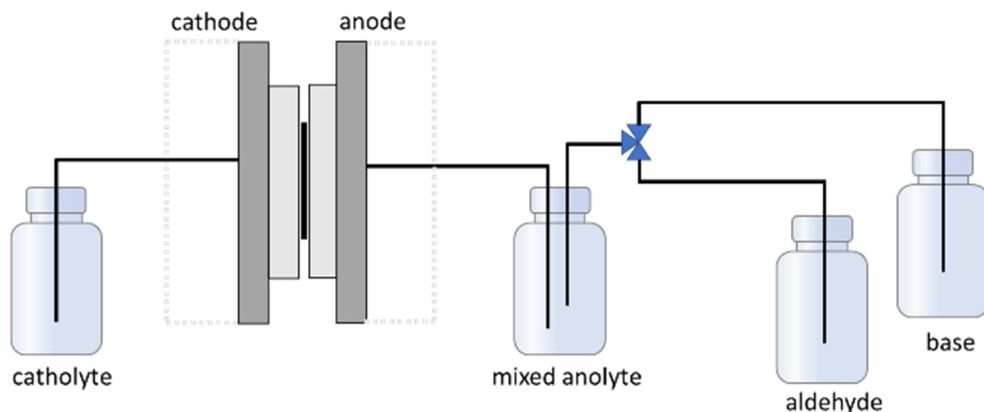


**Fig. S44** Proposed system for bipolar H<sub>2</sub> production to minimize Cannizzaro reaction.

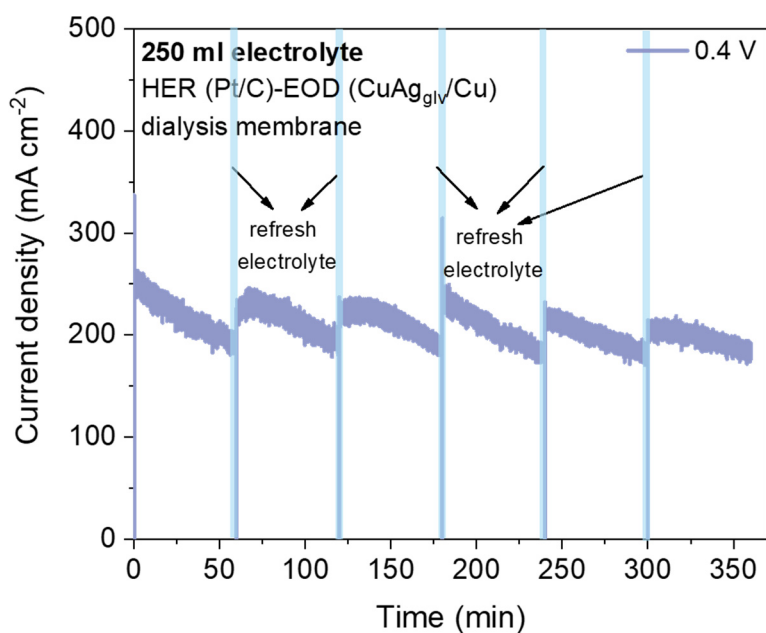


**Fig. S45** 6-hour stability test in the MEA-based system with dialysis membrane at the cell voltage of 0.4 V. A current drop was observed as a result of furfural consumption from EOD reaction and the competitive Cannizzaro reaction. After refreshing the electrolyte (250 mM furfural in 1 M KOH, 250 ml) each hour, the original performance is restored.

## Techno-economic Analysis (TEA) for bipolar H<sub>2</sub> production system

### Assumptions and Methods

This analysis considers the capital and operating costs of a 1500 kg/day H<sub>2</sub> plant to quantify the minimum selling price (MSP) of H<sub>2</sub> and furoic acid. The MSP is defined as the price that yields a net-zero net present value at a 10% internal rate of return over a 20-year period. The economic performance of this system is analyzed by using discounted cash flow rate of return (DCFROR) method developed by the National Renewable Energy Laboratory (NREL).<sup>58</sup> Sensitivity and scenario analysis is conducted to evaluate the impacts of current density, capital cost, separation costs, furfural price, and others. We assumed the electrochemical plant capacity of 1500 kg/day H<sub>2</sub>, based on the hydrogen analysis model developed by the U.S. Department of Energy for producing the same amount of H<sub>2</sub> via water electrolysis.<sup>59</sup> The feedstock input for this study is furfural, and the products are H<sub>2</sub> and furoic acid. The electrolyte is KOH. We considered two scenarios as follows:

- (1) **Scenario 1:** quantifying the MSP of H<sub>2</sub>, with furoic acid as the byproduct to be sold to the market as polyethylene terephthalate (PET). The separation cost of only H<sub>2</sub> was considered.
- (2) **Scenario 2:** quantifying the MSP of furoic acid, with H<sub>2</sub> as the byproduct. The separation cost of both H<sub>2</sub> and furoic acid are considered.

**Table S11** provides the flow rates and prices of the 1500 kg/day H<sub>2</sub> plant for both scenarios. Furfural conversion and recycle ratios were assumed to be 0.5 and 0.99, respectively. The KOH recycle ratio was also assumed to be 0.99. The flowrates of furfural, KOH, and furoic acid and the TEA model are based primarily on assumptions and information provided by Orella et al.<sup>60</sup> **Table S12** depicts the key financial assumptions for this study. The financial assumptions are primarily taken from the PEM electrolysis H<sub>2</sub> production case study and the TEA provided by James et al.<sup>59</sup> and Colella et al.<sup>61</sup>

**Table 11.** Key material, energy flow rates, and prices for an electrochemical plant with the capacity of 1500 kg/day H<sub>2</sub>.

Materials or Energy	Flow rate (MTPD or MWh/day)	Price (\$/MT or \$/KWh)
Furfural*	36.4	-1400 <sup>62</sup>
KOH	42.1	-1000 <sup>63</sup>
Electricity	12	-0.0688 <sup>59</sup>
Process water	16.75	-0.2 <sup>64</sup>
Cooling water	0.62	-1.39 <sup>64</sup>
Compressed inert gas**	34.35	-2.26 <sup>65</sup>
Furoic acid	84.06	600 <sup>66</sup> – Scenario 1
Hydrogen	1.5	3500 <sup>67</sup> – Scenario 2

\*Fresh flow rate required per day after recycling

\*\*Flow rate in Nm<sup>3</sup>/day and corresponding price in \$/Nm<sup>3</sup>

**Table 12.** Key financial assumptions for a 1500 kg/day furfural to H<sub>2</sub> electrochemical plant (adapted from the references<sup>58, 59</sup>)

Parameters	Value	Unit
Operating hours	7900	hours
Project lifetime	20	years
Internal Rate of Return	10	%
Equity	100	%
Construction period	1	years
Replacement interval	10	years
Replacement cost	12	% installed capital cost
Tax rate	39	%
Working capital	1	% of yearly change in operating cost

An electrochemical plant usually comprises two primary sections. The first one is the electrolyzer stack arrangement. The electrolyzer receives furfural as input and produces 2-FA and H<sub>2</sub>. This study included all primary components (bipolar plate, current collector, membrane, end gasket, stack housing, etc.) and corresponding costs (materials, manufacturing, and tooling) involved in manufacturing a stack electrolyzer as reported by James et al.<sup>68</sup> The second section is the balance of plant (BOP), which includes all the ancillary equipment and arrangements required for the proper functioning of the electrolyzer stack section. The BOP costs were taken from Collela et al.<sup>61</sup> The BOP costs primarily included the power electronics devices, sensors, cathode and anode side product management systems, thermal management (TM) and water delivery management (WDM) systems, and finally the mechanical BOP. The mechanical BOP includes costs related to copper cabling, valves, plumbing, labor costs, and other equipment installation expenses.<sup>61</sup>

Experimental data was gathered from this project, and it includes assumptions for catalyst materials and their corresponding loading, and electrolyzer current densities and corresponding cell voltages. **Tables S13 and S14** include all experimental data employed in this analysis. Two cathode catalysts are considered: a Pt/C and Ni<sub>2</sub>P catalyst. The anode employs a CuAg/Cu catalyst. All catalysts were assumed to have a 1 mg/cm<sup>2</sup> loading. Market prices for the catalyst materials are gathered from.<sup>69707172</sup> Catalyst material prices ranged from \$9.34/kg (Cu) to \$33,500/kg (Pt). Cell voltage values considered in the analysis are 0.1, 0.4, 0.6, and 0.8 V. Current densities include 25, 250, and 400 mA/cm<sup>2</sup>.

**Table S13.** Catalyst loading and prices.

Catalyst	Loading (mg/cm <sup>2</sup> )	Price (\$/kg)
Pt/C (Cathode)	1	33500
Ni <sub>2</sub> P (Cathode)	1	19.2
CuAg/Cu (Anode)	1	9.34 (Cu), 721.14 (Ag)

**Table S14.** Current density and cell voltages.

Cell voltage (V)	Current density (mA/cm <sup>2</sup> )	Catalyst (cathode and anode)
0.1	25	Pt/C and CuAg/Cu
0.4	250	
0.6	400	
0.8	400	Ni <sub>2</sub> P and CuAg/Cu

## Detailed calculations

### 1.1 Input and output mass flow rates for 1500 kg/day H<sub>2</sub> plant (for both scenarios)

$$\frac{H_2}{\text{Furfural input}} = \frac{2}{96.08} = \frac{1}{48.04} = \frac{1500 \text{ kg/day}}{72060 \text{ kg/day}}$$

$$\frac{H_2}{\text{KOH input}} = \frac{2}{56.106} = \frac{1}{28.053} = \frac{1500 \text{ kg/day}}{42079.5 \text{ kg/day}}$$

$$\frac{H_2}{\text{Furoic acid output}} = \frac{2}{112.08} = \frac{1}{56.04} = \frac{1500 \text{ kg/day}}{84060 \text{ kg/day}}$$

Mass of furfural and KOH input flow rate required by the plant:

$$[1 - r(1 - c)] * \text{Mass}_{\text{Furfural}} = \text{Mass}_{\text{Furfural\_Plant}}$$

$$(1 - c) * \text{Mass}_{\text{KOH}} = \text{Mass}_{\text{KOH\_Plant}}$$

**Table S15.** Mass flow rates of input and output considered for 1500 kg/day H<sub>2</sub> (for both scenarios)

Parameters	Comments	Values	Units	References
r	recycle rate	0.99	-	60
c	conversion rate	0.5	-	
Mass <sub>Furfural</sub>	mass of furfural going into the electrolyzer	72060	kg/day	This study
Mass <sub>KOH</sub>	mass of KOH going into the electrolyzer	42079.5		
Mass <sub>Furfural Plant</sub>	Mass of furfural required by the plant	36390.3		
Mass <sub>KOH Plant</sub>	Mass of furoic acid required by the plant	420.8		

**Table S16.** Quantification of current required by the 1500 kg/day H<sub>2</sub> plant for both scenarios

$$I = \frac{Q_{mole} * F}{t} = \frac{H_2 \left( \frac{kg}{day} \right) / 24(h)}{2.016 * 10^{-3} (kg/mole) * 96485 \left( \frac{C}{mole} \right)} * 3600 (s)$$

### 1.2 Electrolyzer and BOP costs

The electrolyzer costs were obtained from James et al.<sup>68</sup> and BOP costs were obtained from Orella et al.<sup>60</sup> and Collela et al.<sup>61</sup> for both scenarios.

#### 1.2.1 Electrolyzer Costs

The key components used to make an electrolyzer stack, and their corresponding costs were obtained from James et al.<sup>68</sup> All other resources are mentioned in **Table S17**.

**Table S17.** Electrolyzer stack components considered for the 1500 kg/day H<sub>2</sub> plant

Parameters	Values	Units	References
Bipolar plates	3.70	\$/KW <sub>net</sub>	68
Bipolar plate coating	1.29		
Stack conditioning	0.31		
Gas diffusion layers	5.51		
Hot-pressing process	0.07		
Cutting and slitting procedure	0.03		
Gasket insertion molding	3.17		

End plates	0.27		
Current collector	0.06		
Coolant gasket insertion molding	1.52		
End gasket insertion molding	0.02		
Stack housing	0.07		
Uncatalyzed membrane 1	220 (AEM)	\$/m <sup>2</sup>	<sup>73</sup>
Uncatalyzed membrane 2	50 (Dialysis)	\$/m <sup>2</sup>	<sup>74</sup>

**1.2.2 The total electrolyzer cost** included the materials, manufacturing, and tooling costs of the components used to make the stack. All the stack components were converted to cost per electrolyzer area basis using the following equation:

$$\frac{\$}{A_{\text{stack}}} = \frac{KW_{\text{net}}}{n_{\text{cell}} \times A_{\text{cell}}} \times \frac{\$_{\text{comp}}}{KW_{\text{net}}}$$

**Table S18. Cost of stack components in dollars per area basis.**

Parameters	Comments	Values	Units	References
$KW_{\text{net}}$	net power output	80	kilowatt	<sup>68</sup>
$n_{\text{cell}}$	number of cells	369	-	
$A_{\text{cell}}$	area of each cell	0.024	m <sup>2</sup>	
$\$_{\text{comp}}/KW_{\text{net}}$	cost of each stack component per net power output produced	Depends on the component	\$	
$\$/A_{\text{stack}}$	Cost per electrolyzer stack area	Depends on the component	\$	This study

### 1.3 Separation costs and related flowrates for both scenarios.

**Fig. S46** illustrates the separation procedure after furfural, KOH, H<sub>2</sub>, and furoic acid flow out of the electrolyzer stack for scenarios 1 (left) and 2 (right). At Separator 1, the H<sub>2</sub> gas (both for scenarios 1 and 2) was separated and at Separator 2, furoic acid was separated (for scenario 2). The remaining fluid for both scenarios was recycled back. It was assumed that the conversion rate of furfural (at electrolyzer) was 50%, while the recycling rate of both furfural and KOH was 99%.<sup>60</sup> The separation costs were taken from Orella et al.<sup>60</sup> which followed the Sherwood plot.<sup>75</sup> This plot classified the materials into three sections – (i) gas, (ii) metals, and (iii) biologics. The separation cost is defined as the ratio of separation factor (in \$/kg of the initial amount of components) to initial concentration. The separation factors of H<sub>2</sub> and furoic acid were from Orella et al.<sup>60</sup> as shown in **Table S19**.

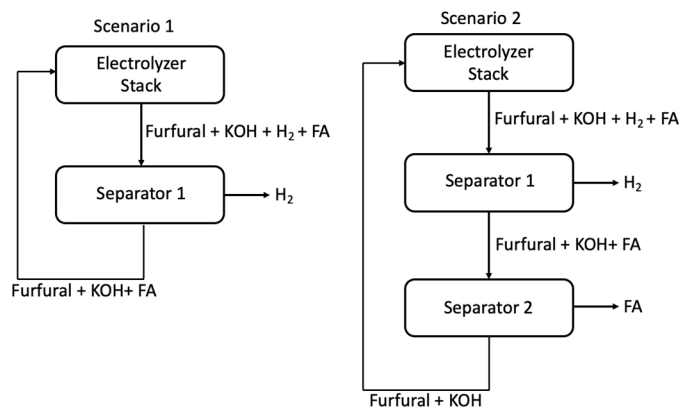


**Fig. S46** Flow diagrams of the separation procedure for Scenario 1 (left) and Scenario 2 (right).

### 1.3.1 Cost of H<sub>2</sub> and furoic acid separation for Scenarios 1 and 2.

Separator 1 is common for both scenarios. Separator 2 is only considered for scenario 2.

$$\text{Sep}_1 = \frac{\varepsilon_{\text{sep-H}_2}}{\frac{\text{H}_2}{\text{H}_2 + \text{FA} + \text{KOH} + \text{furfural}}}$$

$$\text{Sep}_2 = \frac{\varepsilon_{\text{sep-FA}}}{\frac{\text{FA}}{\text{KOH} + \text{furfural}}}$$

**Table S19.** Separation factors and separation costs of the 1500 kg/day H<sub>2</sub>.

Parameters	Value	Units	Reference
Sep <sub>1</sub>	0.11	\$/kg H <sub>2</sub>	This study
ε <sub>sep-H<sub>2</sub></sub>	0.001	\$/kg initial concentration	<sup>60</sup>
Sep <sub>2</sub>	1.9	\$/kg FA	This study
ε <sub>sep-FA</sub>	1	\$/kg initial concentration	<sup>60</sup>

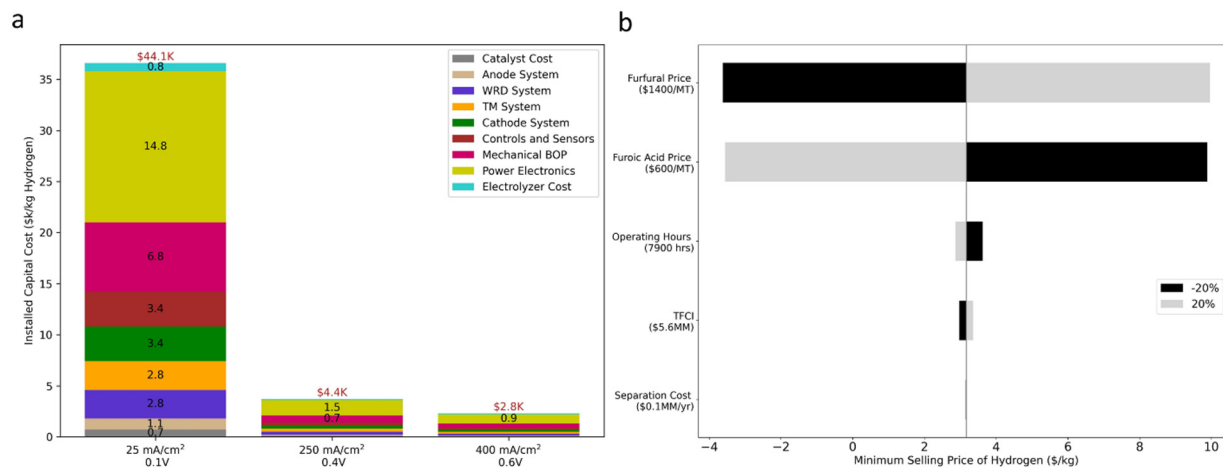


**Fig. S47 Installed capital costs (normalized to \$/kg H<sub>2</sub>) and sensitivity analysis for Scenario 1 in selling of H<sub>2</sub>.** (a) Installed capital costs at various current densities. (b) Sensitivity analysis on key parameters influencing the MSP of H<sub>2</sub> at the base case of 400 mA cm<sup>-2</sup> with cell voltage of 0.6 V. The MEA-based configuration including the AEM, Pt/C cathode, and CuAg/Cu foam anode. The plant capacity is kept constant at 1500 kg/day H<sub>2</sub> from the bipolar H<sub>2</sub> production system.

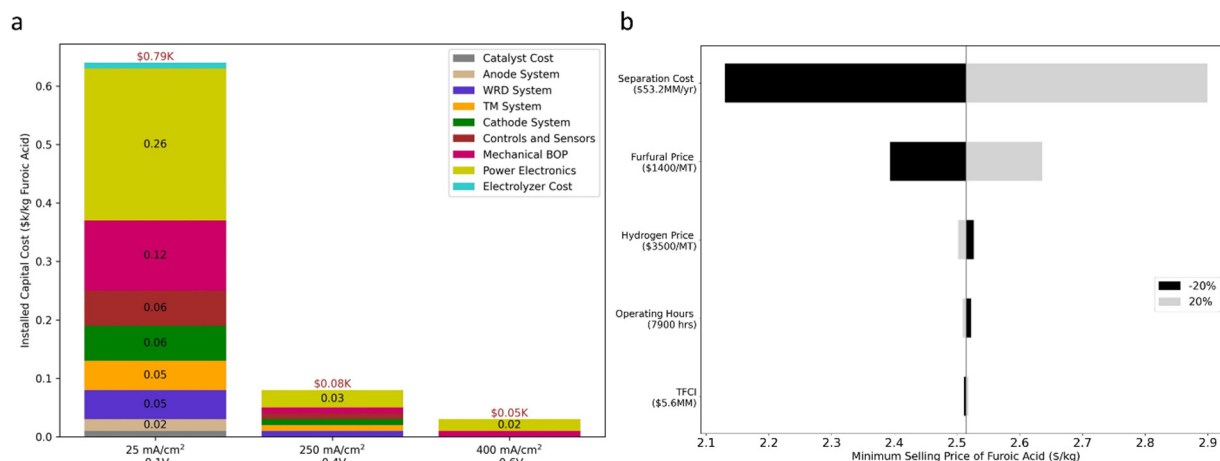


**Fig. S48 Installed capital costs (normalized to \$/kg furoic acid) and sensitivity analysis for Scenario 2 in selling of furoic acid.** (a) Installed capital costs at various current densities. (b) Sensitivity analysis on key parameters influencing the MSP of furoic acid at the base case of 400 mA cm<sup>-2</sup> with cell voltage of 0.6 V. The MEA-based configuration including the AEM, Pt/C cathode, and CuAg/Cu foam anode. The plant capacity is kept constant at 1500 kg/day H<sub>2</sub> from the bipolar H<sub>2</sub> production system.

Unlike scenario 1, it was found that the cost of separating furoic acid was much higher than the cost of separating H<sub>2</sub> gas.

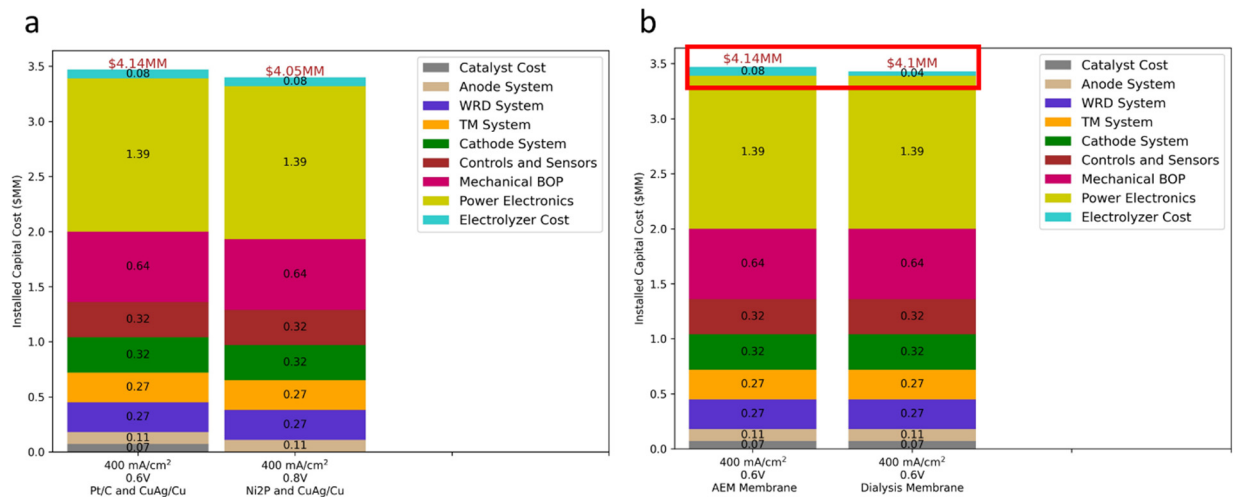


**Fig. S49 Comparison of the total installed capital costs via varying the cathodic catalysts and membranes for both Scenarios 1 and 2.** (a) Total installed capital costs with different cathodic catalysts at a current density of 400 mA/cm<sup>2</sup> with AEM. Based on the experimental results, to attain this same current density, the required voltage in the system with Ni<sub>2</sub>P would be 0.2 V higher than Pt/C. (b) Total installed capital costs with different membranes at a current density of 400 mA/cm<sup>2</sup> with Pt/C cathode. Because the similar membrane resistances, the cell voltage was assumed to be the same of 0.6 V.

It was observed that the electrolyzer cost decreased by ~99% and ~50% by using the cheaper Ni<sub>2</sub>P catalyst and dialysis membrane, respectively. The overall capital cost did not show a significant drop, because the major contribution of the capital cost for electrochemical plant is from the BOP costs instead of electrolyzer cost.

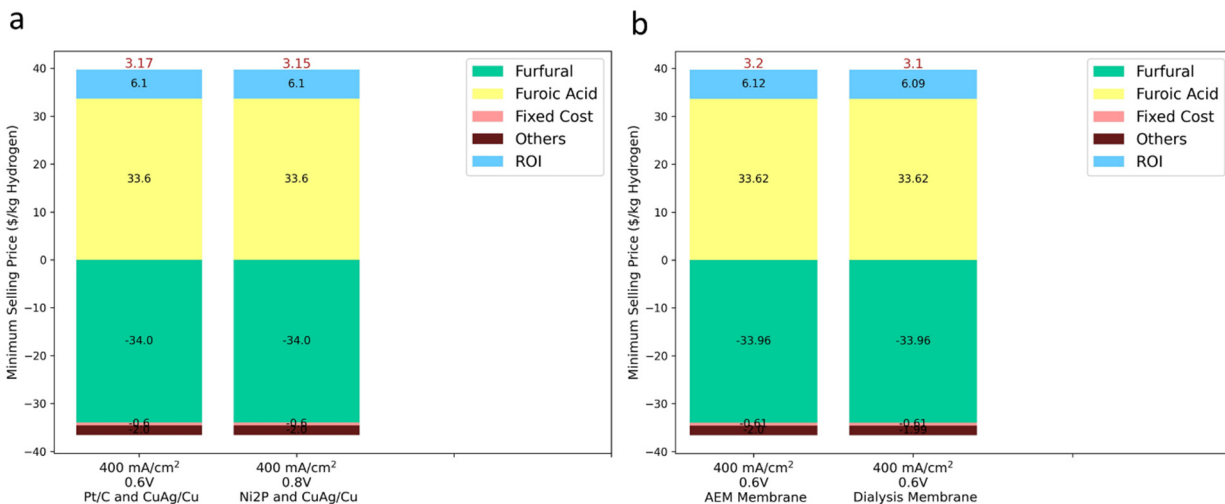


**Fig. S50 Comparison in MSP of H<sub>2</sub> (Scenario 1) for two different sets of catalysts and membranes.** (a) MSP of H<sub>2</sub> in varying the cathodic catalyst. The MSP value increased by around 4.5% when Ni<sub>2</sub>P catalyst was used, because of the increased voltage (0.2 V) to attain 400 mA/cm<sup>2</sup>. This means the cell voltage showed more contribution than catalyst cost in influencing the final MSP. (b) MSP of H<sub>2</sub> in varying the membrane. Membrane cost did not influence the MSP, because the major contributions are from the furfural and furoic acid costs.

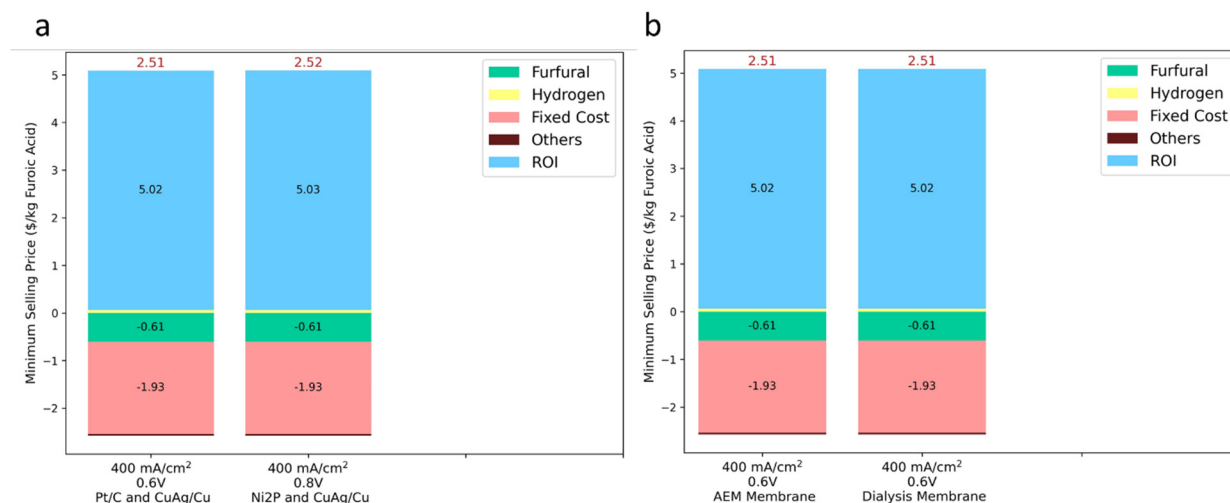


**Fig. S51 Comparison in MSP of furoic acid (Scenario 2) for two different sets of catalysts and membranes.** Similar to Scenario 1, the varying of (a) catalysts and (b) membranes did not significantly influence MSP. This is because the BOP costs dominated more than the electrolyzer costs.

## References

1. S. Lamaison, D. Wakerley, J. Blanchard, D. Montero, G. Rouse, D. Mercier, P. Marcus, D. Taverna, D. Giaume and V. Mougél, *Joule*, 2020, **4**, 395–406.
2. Y. Wang, W. Zhou, R. Jia, Y. Yu and B. Zhang, *Angew. Chem.*, 2020, **132**, 5388–5392.
3. B. Zhang, Y. H. Lui, L. Zhou, X. Tang and S. Hu, *J. Mater. Chem.*, 2017, **5**, 13329–13335.
4. T. F. Fuller and J. N. Harb, *Electrochemical engineering*, John Wiley & Sons, 2018.
5. Q. Duan, S. Ge and C.-Y. Wang, *J. Power Sources*, 2013, **243**, 773–778.
6. A. Reyes, R. P. Jansonius, B. A. Mowbray, Y. Cao, D. G. Wheeler, J. Chau, D. J. Dvorak and C. P. Berlinguette, *ACS Energy Lett.*, 2020, **5**, 1612–1618.
7. P. E. Blöchl, *Phys. Rev. B*, 1994, **50**, 17953.
8. G. Kresse and D. Joubert, *Phys. Rev. B*, 1999, **59**, 1758.
9. J. P. Perdew, J. A. Chevary, S. H. Vosko, K. A. Jackson, M. R. Pederson, D. J. Singh and C. Fiolhais, *Phys. Rev. B*, 1992, **46**, 6671–6687.
10. L. Gong, N. Agrawal, A. Roman, A. Holewinski and M. J. Janik, *J. Catal.*, 2019, **373**, 322–335.
11. A. M. Román, N. Agrawal, J. C. Hasse, M. J. Janik, J. W. Medlin and A. Holewinski, *J. Catal.*, 2020, **391**, 327–335.
12. L. O. Mark, N. Agrawal, A. M. Román, A. Holewinski, M. J. Janik and J. W. Medlin, *ACS Catal.*, 2019, **9**, 11360–11370.
13. J. C. Hasse, N. Agrawal, M. J. Janik and A. Holewinski, *J. Phys. Chem. C*, 2022, **126**, 16, 7054–7065.
14. J. K. Nørskov, J. Rossmeisl, A. Logadottir, L. Lindqvist, J. R. Kitchin, T. Bligaard and H. Jonsson, *J. Phys. Chem. B*, 2004, **108**, 17886–17892.
15. G. Rostamikia, A. J. Mendoza, M. A. Hickner and M. J. Janik, *J. Power Sources*, 2011, **196**, 9228–9237.
16. I. Merino-Jimenez, M. Janik, C. P. De Leon and F. Walsh, *J. Power Sources*, 2014, **269**, 498–508.
17. A. J. Bard and L. R. Faulkner, *Electrochemical methods*, 2001, **2**, 580–632.
18. X. Nie, W. Luo, M. J. Janik and A. Asthagiri, *J. Catal.*, 2014, **312**, 108–122.
19. T. Wang, Z. Huang, T. Liu, L. Tao, J. Tian, K. Gu, X. Wei, P. Zhou, L. Gan and S. Du, *Angew. Chem.*, 2022, **134**, e202115636.
20. D.-H. Nam, B. J. Taitt and K.-S. Choi, *ACS Catal.*, 2018, **8**, 1197–1206.
21. H. Chen, J. Wang, Y. Yao, Z. Zhang, Z. Yang, J. Li, K. Chen, X. Lu, P. Ouyang and J. Fu, *ChemElectroChem*, 2019, **6**, 5797–5801.
22. Y. Zhang, B. Zhou, Z. Wei, W. Zhou, D. Wang, J. Tian, T. Wang, S. Zhao, J. Liu and L. Tao, *Adv. Mater.*, 2021, 2104791.
23. B. Zhou, Y. Zhang, T. Wang, W. Zhou, J. Liu, Y. Zou, L. Tao, Y. Lu and S. Wang, *Chem Catal.*, 2021.
24. M. C. Biesinger, *Surf. Interface Anal.*, 2017, **49**, 1325–1334.
25. P. Sprunger, E. Lægsgaard and F. Besenbacher, *Phys. Rev. B*, 1996, **54**, 8163.
26. P. Subramanian and J. Perepezko, *Journal of Phase Equilibria*, 1993, **14**, 62–75.
27. E. L. Clark, C. Hahn, T. F. Jaramillo and A. T. Bell, *J. Am. Chem. Soc.*, 2017, **139**, 15848–15857.
28. L. Wang, H. Peng, S. Lamaison, Z. Qi, D. M. Koshy, M. B. Stevens, D. Wakerley, J. A. Z. Zeledón, L. A. King and L. Zhou, *Chem Catal.*, 2021, **1**, 663–680.
29. <https://commons.wikimedia.org/wiki/File:Cu-pourbaix-diagram.svg>
30. M. Hans, S. Mathews, F. Mücklich and M. Solioz, *Biointerphases*, 2016, **11**, 018902.
31. I. Platzman, R. Brener, H. Haick and R. Tannenbaum, *J. Phys. Chem. C*, 2008, **112**, 1101–1108.
32. G. Liu, F. Zheng, J. Li, G. Zeng, Y. Ye, D. M. Larson, J. Yano, E. J. Crumlin, J. W. Ager and L.-w. Wang, *Nat. Energy*, 2021, **6**, 1124–1132.
33. D. Frost, A. Ishitani and C. McDowell, *Mol. Phys.*, 1972, **24**, 861–877.
34. S. Anantharaj, H. Sugime and S. Noda, *ACS Appl. Mater. Interfaces*, 2020, **12**, 27327–27338.
35. S. Anantharaj, H. Sugime, S. Yamaoka and S. Noda, *ACS Appl. Energy Mater.*, 2021, **4**, 899–912.
36. N. Jiang, B. You, R. Boonstra, I. M. Terrero Rodriguez and Y. Sun, *ACS Energy Lett.*, 2016, **1**, 386–390.
37. B. You, N. Jiang, X. Liu and Y. Sun, *Angew. Chem. Int. Ed.*, 2016, **55**, 9913–9917.
38. B. You, X. Liu, N. Jiang and Y. Sun, *J. Am. Chem. Soc.*, 2016, **138**, 13639–13646.
39. G. Yang, Y. Jiao, H. Yan, Y. Xie, A. Wu, X. Dong, D. Guo, C. Tian and H. Fu, *Adv. Mater.*, 2020, **32**, 2000455.
40. S.-K. Geng, Y. Zheng, S.-Q. Li, H. Su, X. Zhao, J. Hu, H.-B. Shu, M. Jaroniec, P. Chen and Q.-H. Liu, *Nat. Energy*, 2021, **6**, 904–912.
41. L. Wang, Y. Zhu, Y. Wen, S. Li, C. Cui, F. Ni, Y. Liu, H. Lin, Y. Li and H. Peng, *Angewandte Chemie*, 2021, **133**, 10671–10676.
42. Z. Liu, C. Zhang, H. Liu and L. Feng, *Appl. Catal. B*, 2020, **276**, 119165.
43. Z.-Y. Yu, C.-C. Lang, M.-R. Gao, Y. Chen, Q.-Q. Fu, Y. Duan and S.-H. Yu, *Energy Environ. Sci.*, 2018, **11**, 1890–1897.
44. G.-F. Chen, Y. Luo, L.-X. Ding and H. Wang, *ACS Catal.*, 2018, **8**, 526–530.
45. Y. Zhu, X. Zhu, L. Bu, Q. Shao, Y. Li, Z. Hu, C. T. Chen, C. W. Pao, S. Yang and X. Huang, *Adv. Funct. Mater.*, 2020, **30**, 2004310.
46. Y. Xu, M. Liu, S. Wang, K. Ren, M. Wang, Z. Wang, X. Li, L. Wang and H. Wang, *Appl. Catal. B*, 2021, **298**, 120493.
47. Y. Li, X. Wei, L. Chen, J. Shi and M. He, *Nat. Commun.*, 2019, **10**, 1–12.
48. W.-J. Liu, Z. Xu, D. Zhao, X.-Q. Pan, H.-C. Li, X. Hu, Z.-Y. Fan, W.-K. Wang, G.-H. Zhao and S. Jin, *Nat. Commun.*, 2020, **11**, 1–11.

49. Y. Zhang, B. Zhou, Z. Wei, W. Zhou, D. Wang, J. Tian, T. Wang, S. Zhao, J. Liu and L. Tao, *Adv. Mater.*, 2021, **33**, 2104791.
50. H. Zhao, D. Lu, J. Wang, W. Tu, D. Wu, S. W. Koh, P. Gao, Z. J. Xu, S. Deng and Y. Zhou, *Nat. Commun.*, 2021, **12**, 1–10.
51. D. Wang, N. He, L. Xiao, F. Dong, W. Chen, Y. Zhou, C. Chen and S. Wang, *Angew. Chem.*, 2021, **133**, 24810–24816.
52. B. Zhou, Y. Zhang, T. Wang, W. Zhou, J. Liu, Y. Zou, L. Tao, Y. Lu and S. Wang, *Chem Catal.*, 2021, **1**, 1493–1504.
53. H. Huang, S. Zhou, C. Yu, H. Huang, J. Zhao, L. Dai and J. Qiu, *Energy Environ. Sci.*, 2020, **13**, 545–553.
54. S. Dresp, T. N. Thanh, M. Klingenhof, S. Brückner, P. Hauke and P. Strasser, *Energy Environ. Sci.*, 2020, **13**, 1725–1729.
55. Y. Leng, G. Chen, A. J. Mendoza, T. B. Tighe, M. A. Hickner and C.-Y. Wang, *J. Am. Chem. Soc.*, 2012, **134**, 9054–9057.
56. F. Yu, H. Zhou, Y. Huang, J. Sun, F. Qin, J. Bao, W. A. Goddard, S. Chen and Z. Ren, *Nat. Commun.*, 2018, **9**, 1–9.
57. T. Wang, L. Tao, X. Zhu, C. Chen, W. Chen, S. Du, Y. Zhou, B. Zhou, D. Wang and C. Xie, *Nat. Catal.*, 2021, 1–8.
58. E. C. Tan, M. Talmadge, A. Dutta, J. Hensley, J. Schaidle, M. Biddy, D. Humbird, L. J. Snowden-Swan, J. Ross and D. Sexton, *Process Design and Economics for the Conversion of Lignocellulosic Biomass to Hydrocarbons via Indirect Liquefaction. Thermochemical Research Pathway to High-Octane Gasoline Blendstock Through Methanol/Dimethyl Ether Intermediates*, National Renewable Energy Lab.(NREL), Golden, CO (United States), 2015.
59. B. James, W. Colella, J. Moton, G. Saur and T. Ramsden, *PEM electrolysis H2A production case study documentation*, National Renewable Energy Lab.(NREL), Golden, CO (United States), 2013.
60. M. J. Orella, S. M. Brown, M. E. Leonard, Y. Román-Leshkov and F. R. Brushett, *Energy Technol.*, 2020, **8**, 1900994.
61. W. G. Colella, B. D. James, J. M. Moton, G. Saur and T. Ramsden, 2014.
62. G. H. Dubbink, T. R. Geversink, B. Haar, H. W. Koets, A. Kumar, H. van den Berg, A. G. van der Ham and J. P. Lange, *Biofuels, Bioproducts and Biorefining*, 2021.
63. Science Company-Lab Grade Flake Potassium Hydroxide. Available from: <https://www.sciencecompany.com/Potassium-Hydroxide-500g-P6511.aspx>
64. M. R. Rover, A. Aui, M. M. Wright, R. G. Smith and R. C. Brown, *Green Chem.*, 2019, **21**, 5980-5989.
65. Prices for Compressed Gases [Internet]. Available from: <https://procurement.umbc.edu/files/2013/10/AirgasExp04302015.pdf>
66. Bottle Grade PET Resin Polyethylene Terephthalate Factory supplies Transparent Film plastic raw Fiber, alibaba.com, accessed 6 January 2022 [Internet]. Available from: [https://www.alibaba.com/product-detail/Bottle-Grade-PET-Resin-Polyethylene-Terephthalate\\_1600384501791.html?spm=a2700.galleryofferlist.normal\\_offer.d\\_title.4ed82a61mLCRrb&s=p](https://www.alibaba.com/product-detail/Bottle-Grade-PET-Resin-Polyethylene-Terephthalate_1600384501791.html?spm=a2700.galleryofferlist.normal_offer.d_title.4ed82a61mLCRrb&s=p)
67. G. Saur and C. Ainscough, *US Geographic analysis of the cost of hydrogen from electrolysis*, National Renewable Energy Lab.(NREL), Golden, CO (United States), 2011.
68. B. D. James, J. M. Huya-Kouadio, C. Houchins and D. A. DeSantis, *Mass Production Cost Estimation of Direct H2 PEM Fuel Cell Systems for Transportation Applications (2012-2016)*, Strategic Analysis Inc., Arlington, VA (United States), 2016.
69. Markets Insider-Silver Price Today, accessed 25 September 2021 [Internet]. Available from: <https://markets.businessinsider.com/commodities/silver-price>
70. Markets Insider-Nickel Price Today, accessed 2 October 2021 [Internet]. Available from: <https://markets.businessinsider.com/commodities/nickel-price>
71. Markets Insider-Copper Price Today, accessed 25 September 2021 [Internet]. Available from: <https://markets.businessinsider.com/commodities/copper-price>
72. Markets Insider-Silver Price Today, accessed 25 September 2021 [Internet]. Available from: <https://markets.businessinsider.com/commodities/silver-price>
73. Paper W. INNOVATIONS Hydrogen Production Cost by AEM Water Electrolysis [Internet]. 2020. Available from: [www.ionomr.com](http://www.ionomr.com)
74. T. Janoschka, N. Martin, U. Martin, C. Friebe, S. Morgenstern, H. Hiller, M. D. Hager and U. S. Schubert, *Nature*, 2015, **527**, 78–81.
75. J. B. Dahmus and T. G. Gutowski, *Environ. Sci. Technol.*, 2007, **41**, 7543–7550.